The Accuracies of Smoothed Sea Surface Height Fields Constructed from Tandem Satellite Altimeter Datasets

DUDLEY B. CHELTON AND MICHAEL G. SCHLAX

College of Oceanic and Atmospheric Sciences, Oregon State University, Corvallis, Oregon

ABSTRACT

A technique previously developed for assessing the effects of sampling errors on sea surface height (SSH) fields constructed from satellite altimeter data is extended to include measurement errors, thus providing estimates of the total mean-squared error of the SSH fields. The measurement error contribution becomes an important consideration with the greater sampling density of a coordinated tandem satellite mission. Mean-squared errors are calculated for a variety of tandem altimeter sampling patterns. The resolution capability of each sampling pattern is assessed from a subjectively chosen but consistent set of criteria for the mean value and the spatial and temporal inhomogeneity of the root-mean-squared errors computed over a representative large collection of estimation times and locations.

For a mean mapping error threshold tolerance criterion of 25% of the signal standard deviation, the filter cutoff wavelength and period defining the resolution capability of SSH fields constructed from a tandem TOPEX/ Poseidon (T/P) and *Jason* satellite sampling pattern with evenly spaced ground tracks are about 2.2° by 20 days. This can be compared with the resolution capability of about 6° by 20 days that can be obtained from a single altimeter in the T/P orbit. A tandem T/P–*Jason* mission with 0.75° spacing between simultaneously sampled parallel tracks that has been suggested for estimating geostrophic velocity yields an SSH mapping resolution capability of about 3.7° by 20 days. For the anticipated factor-of-2 larger orbit errors for *ENVISAT* compared with *Jason,* the resolution capability of a tandem *Jason–ENVISAT* scenario is about 3° by 20 days.

For mapping the SSH field, the tandem T/P–*Jason* sampling patterns with evenly spaced, interleaved ground tracks and either a 5-day or a 0-day offset is far better than the other tandem altimeter mission scenarios considered here. For the highest-resolution mapping, the 5-day offset is preferable to the 0-day offset. The scientific benefits of such a tandem mission are discussed in the context of two specific examples: Rossby wave dispersion and investigation of eddy–mean flow interaction.

1. Introduction

The launch of the *Jason* altimeter satellite in December 2001 offers the first opportunity for a coordinated tandem satellite mission for high-quality altimeter measurements of sea surface height (SSH). TOPEX/Poseidon (T/P) established a 10-yr record of SSH measurements from a 10-day exact-repeat orbit with an inclination of 66°, for which neighboring ground tracks are separated by 2.834° of longitude. The *Jason* altimeter satellite was launched into the same orbit as T/P, thus continuing the 10-yr record of SSH along the T/P ground tracks. After an initial 7-month calibration and validation phase, it became possible for the first time to establish a coordinated tandem sampling pattern. By maneuvering T/P into a different 10-day exact-repeat orbit with the same 66° inclination, SSH could be measured along a ground track pattern with a wide range of pos-

sible separations longitudinally and temporally relative to the ground track pattern sampled during the first 10 years of the T/P mission. Another opportunity for a coordinated tandem mission will become available after the launch of the *Jason* follow-on altimeter satellite that is presently planned for 2007. The objective of this study is to investigate what tandem orbit configuration best satisfies the needs of scientific studies of SSH variability.

The most intuitive tandem sampling pattern for mapping the SSH field is an interleaved orbit consisting of evenly spaced ground tracks with a longitudinal separation of 1.417°. This sampling pattern would also provide a quadrupling of the grid of crossover points at which estimates of the zonal and meridional components of the surface geostrophic velocity field could be obtained by the crossover method (Morrow et al. 1992, 1994; Schlax and Chelton 2003). The crossover points would consist of a latitudinally staggered grid with a 1.417° longitudinal spacing and an approximate 1.5° latitudinal spacing at midlatitudes. Stammer and Dieterich (1999) devised an alternative to the crossover

Corresponding author address: Dudley B. Chelton, College of Oceanic and Atmospheric Sciences, Oregon State University, 104 Ocean. Admin. Building, Corvallis, OR 97331-5503.
E-mail: chelton@coas.oregonstate.edu

method that would utilize SSH data obtained from parallel ground tracks. This method would allow velocity estimates to be obtained at closely spaced intervals along tracks, with the goal of resolving short-scale features of the flow field and possibly yielding high-resolution along-track wavenumber spectra of geostrophic velocity variability. Estimates of orthogonal components of geostrophic velocity are obtained with this proposed parallel-track method from between-track differences of SSH. From simulations based on the characteristics of T/P measurement errors, the optimal tandem T/P–*Jason* mission for parallel-track estimation of geostrophic velocity is one for which the ground tracks are offset by a longitudinal shift of 0.75° (Leeuwenburgh and Stammer 2002; Schlax and Chelton 2003). A closer track spacing amplifies the effects of measurement and orbit errors on estimates of the along-track component of geostrophic velocity and a wider track spacing increases sampling errors from unresolved mesoscale variability with spatial scales shorter than the track spacing.

The errors in velocity estimates from both the crossover and parallel-track methods have been compared through simulations based on a high-resolution ocean circulation model (Leeuwenburgh and Stammer 2002) and by analytical means (Schlax and Chelton 2003). Leeuwenburgh and Stammer (2002) conclude that the parallel-track method is capable of providing velocity estimates with errors that are at least as small as, and possibly smaller than, those from the crossover method. Schlax and Chelton (2003) argue that estimates from both methods are subject to substantial errors and neither is clearly superior with regard to the magnitude of the estimation errors. Schlax and Chelton (2003) also caution that the effects of latitudinally varying filtering and estimation errors that are inherent in the parallel-track method need further study before its use for high-resolution along-track wavenumber spectral analyses can be recommended.

After much deliberation, including consideration of the results presented in this paper, the tandem mission that was adopted for T/P and *Jason* consists of interleaved orbits with evenly spaced ground tracks separated by 1.417° of longitude with 7-min offset between adjacent tracks (referred to here as a 0-day offset). This tandem sampling pattern was established on 16 September 2002. After the launch of the *Jason* follow-on altimeter planned for 2007, it will be possible to consider alternative tandem orbit configurations such as the 0.75° track separation suggested by Leeuwenburgh and Stammer (2002). In addition to the estimation of geostrophic velocity considered by Leeuwenburgh and Stammer (2002) and Schlax and Chelton (2003), a decision to commit to a future tandem altimeter mission with 0.75° track separation should consider the impact of this sampling pattern on the ability to map SSH. The primary goal of this paper is to compare the SSH mapping resolution capabilities of a tandem T/P–*Jason* altimeter mission with 0.75° track spacing and two tandem T/P–

Jason missions with evenly spaced ground tracks, one with 5-day offset and the other with the 0-day offset between adjacent tracks adopted for the present tandem T/P–*Jason* mission.

The paper is organized as follows. The details of the method used to assess the resolution capability from estimates of the mapping errors in SSH fields constructed from altimeter data are summarized in section 2. The analyses of the effects of sampling errors considered previously by Chelton and Schlax (1994) and Greenslade et al. (1997) are extended here to include measurement and orbit errors. While the measurement error contribution is relatively small compared with sampling errors for a single altimeter, measurement errors become more important with the greater sampling density of tandem altimeter missions, especially when the orbit errors are large. The present analysis is also based on a more accurate representation of the spatial autocorrelation function of global SSH variability than was used in our earlier studies. The method is applied in sections 3a–c to determine the SSH mapping resolution capability of a single altimeter in the T/P orbit and the tandem T/P–*Jason* sampling patterns described above.

Given the availability of SSH data from *ENVISAT* (a successor to the *ERS-1* and *ERS-2* satellites), we also investigate in section 3d the mapping errors in SSH fields constructed from the tandem *Jason–ENVISAT* sampling pattern as a possible alternative for obtaining high-resolution SSH fields. The effects of measurement errors become especially important when considering the *ENVISAT* data, for which the orbit errors are expected to be approximately double the orbit errors of T/P and *Jason.*

It will be concluded that a tandem T/P–*Jason* sampling pattern with evenly spaced ground tracks and a 5-day offset between the adjacent tracks offers the best option for a tandem orbit configuration in terms of mapping the SSH field. The accuracy of SSH fields constructed from this tandem ground track pattern is degraded somewhat when the offset between adjacent tracks is reduced to zero days, as in the present tandem T/P–*Jason* mission. The degradation becomes almost imperceptible, however, for smoothing of more than 2° × 2° × 20 days. The scientific benefits of these tandem T/P–*Jason* sampling patterns with evenly spaced ground tracks are discussed in section 4 in the context of two specific examples: investigation of the wavenumber-frequency dispersion characteristics of oceanic Rossby waves from SSH fields, and analysis of surface geostrophic velocity to investigate the effects of eddy Reynolds stresses on the mean and slowly varying ocean circulation. These applications are both important to understanding ocean dynamics. Neither topic can be addressed adequately from the sampling pattern of a single altimeter in the T/P orbit.
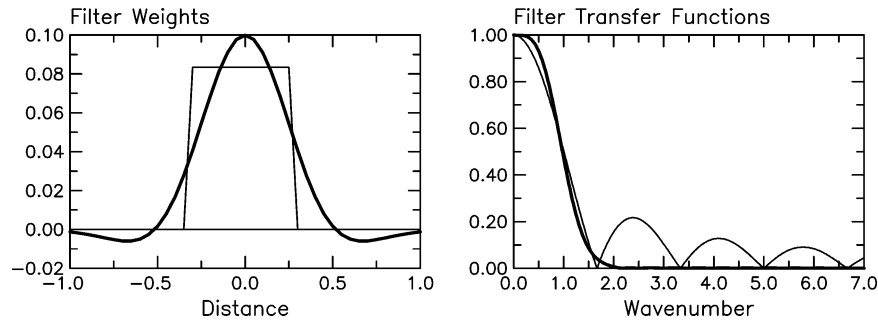
FIG. 1. (left) The weighting functions and (right) filter transfer functions for the loess smoother with a nondimensionalized half-span of one (heavy lines) and a boxcar average with a nondimensionalized full-span of 0.6 (thin lines).

2. Methodology

A technique for assessing the effects of sampling errors on SSH fields constructed from an irregularly sampled dataset was developed by Schlax and Chelton (1992) (referred to hereafter as SC92) and has been applied to altimeter data by Chelton and Schlax (1994) and Greenslade et al. (1997) (referred to hereafter as CS94 and GCS97, respectively). The method is based on a formalism that quantifies the filtering properties of any linear interpolation or smoothing algorithm applied to an arbitrary spatial and temporal distribution of observations. The filter transfer function for a given estimate is compared with an idealized "boxcar" low-pass filter that passes 100% of the variability at wavenumbers and frequencies below specified cutoff values and attenuates all of the variability at higher wavenumbers and frequencies. The mean squared error of an estimate of smoothed SSH is derived from the imperfections of the filter transfer function and the spectral characteristics of the signal and measurement errors [see Eq. (2) below].

A practical difficulty of the SC92 technique is the necessity for the evaluation of improper, three-dimensional integrals. These computations become infeasible when calculating the sampling errors for a broad range of spatial and temporal smoothing parameters at a large number of estimation times and locations. CS94 and GCS97 addressed this practical limitation by estimating the sampling errors at only two estimation locations (a crossover and a diamond center at a middle latitude) and at a small number of estimation times, and by replacing the full integration with a Monte Carlo approximation.

Schlax et al. (2001) (referred to hereafter as SCF01) recently developed a modified approach to estimating the sampling errors for a specific linear interpolation and smoothing algorithm: the quadratic loess smoother introduced by Cleveland and Devlin (1988), which consists of a weighted least squares fit to a quadratic surface in space and time (see also SC92 and appendix B of GCS97). The integral necessary to estimate the errors of quadratic loess estimates can be evaluated analyti-

cally if the tricubic weighting function of the Cleveland and Devlin (1988) algorithm is replaced with a Gaussian weighting function[1] and the filter transfer function for the irregular sampling pattern is compared with the best achievable filter transfer function, rather than the idealized perfect boxcar filter transfer function. The "best achievable filter transfer function" is the transfer function that would exist for the quadratic loess smoother if the observations were continuously distributed in space and time.

As in our previous studies, the filtering properties of the modified loess smoother are characterized here by the filter cutoff wavenumbers and frequencies corresponding to the half-power points of the filter transfer function in longitude, latitude, and time. The Gaussian weighted loess smoother used here was calibrated so that these half-power points are approximately equal to the half spans in space and time over which the data are fit to a quadratic surface. It is thus straightforward to control the filtering properties of the loess smoother by a priori specification of the spatial and temporal spans of the smoother. For comparison with the more familiar linear smoother consisting of a simple block average in space and time, a quadratic loess estimate with filter cutoffs of 3° in longitude and latitude by 10 days, for example, is approximately equivalent to the filter cutoffs of a block average over 1.8° in longitude and latitude by 6 days (see Fig. 1; see also Figs. 4 and 6 of SC92). The sidelobes of the filter transfer functions are quite large for the block average and virtually nonexistent for the quadratic loess smoother, rendering the block averaging method much less efficient as a low-pass filter.

The ability to evaluate the integrals analytically with the SCF01 method allows estimates of the sampling errors at a large number of estimation times and locations with a broad range of smoothing parameters. The estimated sampling errors are smaller than those obtained by the earlier methodology (typically by about

---

[1] The differences between loess smoothed estimates obtained with tricubic vs Gaussian weighting functions are almost indistinguishable (see the filter transfer functions in Fig. 9 of SCF01).

50%) because the actual filter transfer function for irregularly sampled observations is always more similar to the best achievable filter transfer function than it is to the idealized boxcar filter transfer function (see Fig. 9 of SCF01). Except in magnitude, however, the patterns of the sampling errors are very similar from the two methods. Both methods therefore lead to generally the same conclusion regarding the relative contributions of sampling errors to the accuracies of SSH fields constructed with a variety of smoothing parameters.

The previous studies by CS94 and GCS97 addressed only the effects of sampling errors. For SSH fields constructed from measurements with the higher sampling density of tandem satellite datasets, it becomes important to consider also the effects of measurement errors. For the case of altimeter data, orbit errors are of greatest concern. The orbit errors for T/P are 2–3 cm (Chelton et al. 2001) and early analysis indicates that the orbits for *Jason* are accurate to even better than 2 cm (John Ries 2002, personal communication). In comparison, because of its lower orbit altitude and the larger physical size of the satellite, the orbit errors for *ENVISAT* are expected to be about a factor of 2 larger than the T/P and *Jason* orbit errors. It will be seen that these larger orbit errors have a significant impact on the accuracy of SSH fields constructed from *ENVISAT* data.

To investigate the importance of measurement and orbit errors, the previous studies of sampling errors are extended here to consider the mean-squared error (mse) of an estimate $\hat{h}$ of the best possible estimate $\overline{h}$ of smoothed SSH that would be obtained by the quadratic loess smoother if the observations were continuously distributed in space and time. This differs from the more traditional characterization of the error relative to the total (unsmoothed) SSH that is considered in optimal interpolation (e.g., Le Traon and Dibarboure 1999). The mse of smoothed SSH can be written as

$$\langle(\hat{h} - \overline{h})^2\rangle = \langle(\hat{h} - \langle\hat{h}\rangle)^2\rangle + \langle(\overline{h} - \langle\hat{h}\rangle)^2\rangle, \quad (1)$$

where the angle brackets denote the expected value. The first and second terms on the right side of this equation are, respectively, the measurement error variance and the expected squared bias of $\hat{h}$. The effects of sampling errors are wholly embodied in the expected squared bias term. The contributions of measurement and orbit errors to the mean squared error are contained in the variance term. As shown in CS94 and GCS97, (1) can be expressed as

$$\langle(\hat{h} - \overline{h})^2\rangle = \int_{-\infty}^{\infty}\int_{-\infty}^{\infty}\int_{-\infty}^{\infty} |\Delta\hat{P}|^2 S_{\mathrm{err}}(k, l, f)\, dk\, dl\, df$$
$$+ \int_{-\infty}^{\infty}\int_{-\infty}^{\infty}\int_{-\infty}^{\infty} |\Delta\hat{P}|^2 S_h(k, l, f)\, dk\, dl\, df,$$
$$(2)$$

where k and l are the zonal and meridional wavenumbers, f is frequency, S_h and S_{err} are the wavenumber-frequency power spectral densities of the SSH and the measurement errors, and $\Delta\hat{P}(k, l, f)$ is the wavenumber-frequency dependence of the imperfections of the filter transfer function. As noted above, $\Delta\hat{P}$ is defined here to be the differences between the filter transfer function for the particular irregular sampling pattern and the best achievable filter transfer function that would be obtained if the observations were continuously distributed in space and time.

The quality of an individual estimate is quantified here by the root-mean-squared error (rmse), which is the square root of (2) and will also be referred to herein as as the ''mapping error.'' To calculate the expected squared bias contribution [the second term on the right side of (2)], it is necessary to specify the wavenumber-frequency spectrum of SSH, or equivalently, the space–time autocorrelation function and variance of SSH. A further restriction for evaluating the expected squared bias analytically by the method of SCF01 is the requirement that the autocorrelation function have the form of a Gaussian multiplied by a polynomial with only constant and second degree terms. The polynomial terms allow for zero crossings of the autocorrelation, which may be an important feature in some applications of the methodology.

In our previous assessments of the effects of sampling errors (CS94 and GCS97), we have focused on the estimation of SSH at midlatitudes where a Gaussian autocorrelation function with an *e*-folding decorrelation scale of 50 km was assumed. For the wide range of latitudes to be considered here, the general equatorward increase in the spatial decorrelation scale of SSH variability must be taken into consideration. Stammer (1997) presented a global, latitudinally varying correlation function for SSH with a decorrelation scale that is linearly related to the Rossby radius of deformation. His analytical function representation appears to provide a good description of the spatial correlation of SSH [see Fig. 26b and Eqs. (13) and (19) in Stammer (1997)]. However, the function is not positive definite in either one or two dimensions (which may be demonstrated by direct numerical calculation of its Fourier and Hankel transforms) and is therefore not useful for calculating mapping errors (Bretherton et al. 1976). For the functional representation required by the method of SCF01, we were not able to obtain positive definite approximants with the specified zero crossing for the autocorrelation functions presented by Stammer (1997).

For the purposes of this study, we have assumed a simple Gaussian spatial autocorrelation function for SSH with spatial *e*-folding decorrelation scale chosen to match the latitudinally varying spatial decorrelation scales of the function proposed by Stammer (1997) and based on the Rossby radii calculated by Chelton et al. (1998). As shown in Fig. 2, the spatial autocorrelation of SSH for the analysis presented here has longer decorrelation scale at all latitudes (especially in the Tropics) than the midlatitude 50-km decorrelation scale con-
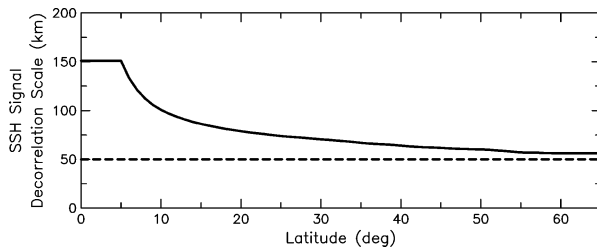
FIG. 2. The latitudinally varying spatial decorrelation scale of sea surface height used in this study. The dashed line shows the 50-km spatial decorrelation scale assumed by Chelton and Schlax (1994) and Greenslade et al. (1997).

sidered by CS94 and GCS97. As a result, the spatial resolution capabilities of the altimeter sampling patterns are correspondingly slightly better at midlatitudes in the analyses presented here than in our previous assessments of midlatitude resolution capability. CS94 and GCS97 did not consider the resolution capability in tropical or subpolar latitudes.

As in CS94 and GCS97, we have assumed a Gaussian temporal autocorrelation function with an e-folding decorrelation scale of 30 days (Shen et al. 1986; Stammer 1997).

For presentation purposes, we have further assumed that SSH has a signal standard deviation of 10 cm. As discussed at the end of this section, the results presented here are easily scaled to obtain rmse for arbitrary signal standard deviations. The wavenumber-frequency distribution of the signal variance is specified by the wavenumber-frequency spectrum of the Gaussian form assumed here for the space–time autocorrelation function of SSH.

The variance contribution to the mean squared error [the first term on the right side of (2)] depends on the wavenumber-frequency spectrum, or equivalently, the space–time covariance function of the altimeter measurement errors. The SSH data are assumed here to be contaminated by two types of measurement error: random instrumental errors ϵ and long-wavelength measurement and orbit errors o. The first are assumed to be uncorrelated between measurements with a variance of σ_ϵ^2. This error process thus has a covariance matrix with σ_ϵ^2 on the diagonal and zeros elsewhere. The long-wavelength measurement and orbit errors are assumed to have variance σ_o^2 and a Gaussian autocorrelation function with a decorrelation timescale of 30 min, reflecting an assumption that these errors have long along-track length scales but are uncorrelated between neighboring ground tracks and between different repeats of a given ground track. The off-diagonal terms in the covariance matrix for these long-wavelength errors are therefore nonzero. We assume that the measurement error components ϵ and o are uncorrelated, so that the total covariance matrix for the errors is the sum of the individual matrices.

For the calculations here, the random instrumental

measurement errors for T/P, *Jason,* and *ENVISAT* are all assumed to have a standard deviation of $\sigma_\epsilon = 2$ cm, which is a slightly conservative approximation of the 1.7-cm T/P instrumental measurement errors (Chelton et al. 2001). For T/P and *Jason,* we assume that the long-wavelength measurement and orbit errors have a standard deviation of $\sigma_o = 2$ cm, which factors in anticipated continued improvements in precision orbit determination over the present orbit accuracy of about 2.5 cm. For *ENVISAT,* we consider the cases of long-wavelength measurement and orbit errors with standard deviations of $\sigma_o = 4$ and 6 cm.

Because of the complicated space–time characteristics of satellite sampling patterns, the rmse at a particular location typically varies considerably over the period of an exact-repeat orbit, especially for small spatial and temporal smoothing of the data. Likewise, the rmse for a particular time typically varies considerably over the mapping area; examples are shown below. When these spatial and temporal inhomogeneities of the mapping errors are large, they can result in artifacts in the SSH fields that might be misinterpreted as real oceanographic features (see Figs. 6 and 7 below). Since the rmse for any linear estimate can be calculated for any time and location in the mapping domain, it is possible to restrict analysis of smoothed and gridded SSH fields to the times and locations where the rmse is deemed to be acceptably small. In practice, however, such selective analysis is seldom implemented. A preferred approach for most applications is to select the smoothing parameters so that the overall average rmse and the spatial and temporal inhomogeneities of the rmse are both reduced to acceptably small levels.

The quality of SSH fields constructed from the various altimeter sampling patterns considered here is assessed from the overall average and the spatial and temporal variability of rmse values calculated over a representative collection of estimation times and locations. Our previous assessments of the resolution capability of altimeter sampling patterns (CS94 and GCS97) characterized the spatial and temporal inhomogeneity of mapping errors by the maximum deviation from the mean mapping error. This metric is replaced here by the 90% quantile range of variation in a histogram of rmse values, that is, the range that encompasses the central 90% of the distribution of rmse values. For the 10-day sampling patterns of T/P and *Jason,* the two measures of inhomogeneity of mapping errors lead to essentially the same conclusions. For the longer 35-day repeat of the ERS and *ENVISAT* orbits, however, the rmse variability criterion adopted here is more "forgiving" in the sense that it leads to more liberal estimates of the resolution capability because of the long-tailed nature of the distributions of rmse values (see section 3d).

For the analyses in section 3, we adopt somewhat arbitrary values of 2.5 and 1.0 cm as thresholds of acceptable average and 90% quantile values of rmse for the smoothed fields constructed from altimeter-sampled
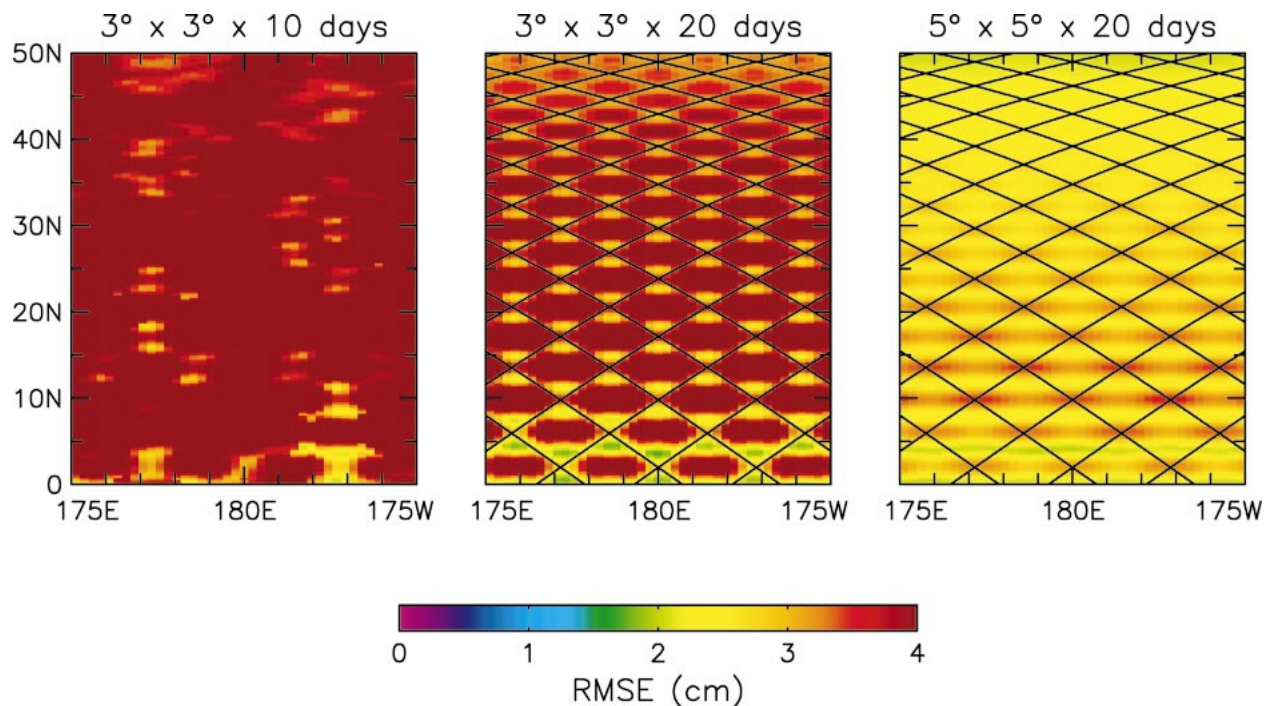
FIG. 3. Rmse of SSH constructed from measurements from a single altimeter in the T/P orbit for the zonal, meridional and temporal filter cutoffs indicated at the top of each panel. The calculations assume Gaussian autocorrelation functions with an *e*-folding temporal scale of 30 days, the latitudinally varying spatial *e*-folding scale shown in Fig. 2, and an SSH signal variance of 10 cm. When multiplied by 10, these rmse can be interpreted as percentages of an arbitrary signal standard deviation. The T/P ground tracks are overlaid on the middle and right panels.

SSH with the total signal standard deviation of 10 cm assumed here. The results presented here are easily generalized to mapping of SSH variability with arbitrary signal standard deviation. When multiplied by 10, the rmse presented in section 3 can be interpreted as percentages of the signal standard deviation. The threshold values of 2.5 and 1.0 cm for the mean and 90% quantile values of rmse thus correspond to 25% and 10% of an arbitrary signal standard deviation. The conclusions about the relative mapping resolution capabilities of the various altimeter sampling patterns are not strongly sensitive to the precise values adopted for these threshold parameters.

The method used here to assess the resolution capability of an altimeter sampling pattern thus strives to produce SSH fields on a fine space–time grid with relatively homogeneous mapping errors. This approach differs from that developed by Tai (1998). For estimates of SSH at the midpoints along the ground tracks halfway between each crossover, he is able to quantify the Nyquist wavelengths and period below which the SSH variability is unresolved and aliases into the SSH estimates. The zonal and meridional Nyquist wavelengths are, respectively, the zonal and meridional spacings of the crossover points, and the aliasing period is twice the exact-repeat period of the satellite orbit. For the T/P orbit, the zonal spacing of crossovers is 2.834° of longitude and the latitudinal spacing decreases from about

8° at the equator to about 1° at 60° latitude (see Fig. 4 of GCS97). The midlatitude resolution capability deduced by Tai (1998) for SSH at the midpoints is thus about 3° of longitude by 6° of latitude by 20 days. In more recent developments, Tai (2001) suggests that the resolution capability of the midpoints is also the resolution capability of the entire dataset.

3. Mapping errors in SSH fields

a. A single altimeter in the T/P orbit

As a benchmark for comparison with the tandem orbit configurations considered in sections 3b–d, we first summarize the mapping errors in SSH fields constructed from a single altimeter in the T/P orbit. Example maps of rmse are shown in Fig. 3 for three selected combinations of spatial and temporal filter cutoffs. For these calculations, the rmse was computed on a 0.25° grid over the geographical domain shown in the figures for a specific estimation time during the T/P 10-day repeat period. The error maps differ somewhat for different estimation times, especially for small smoothing parameters. The errors for the case of 3° by 10-day smoothing (left panel) are far in excess of 4 cm over most of the region. Increasing the temporal smoothing to 20 days (middle panel) reduces the errors to less than 3 cm near the crossover locations, but errors are still in excess of
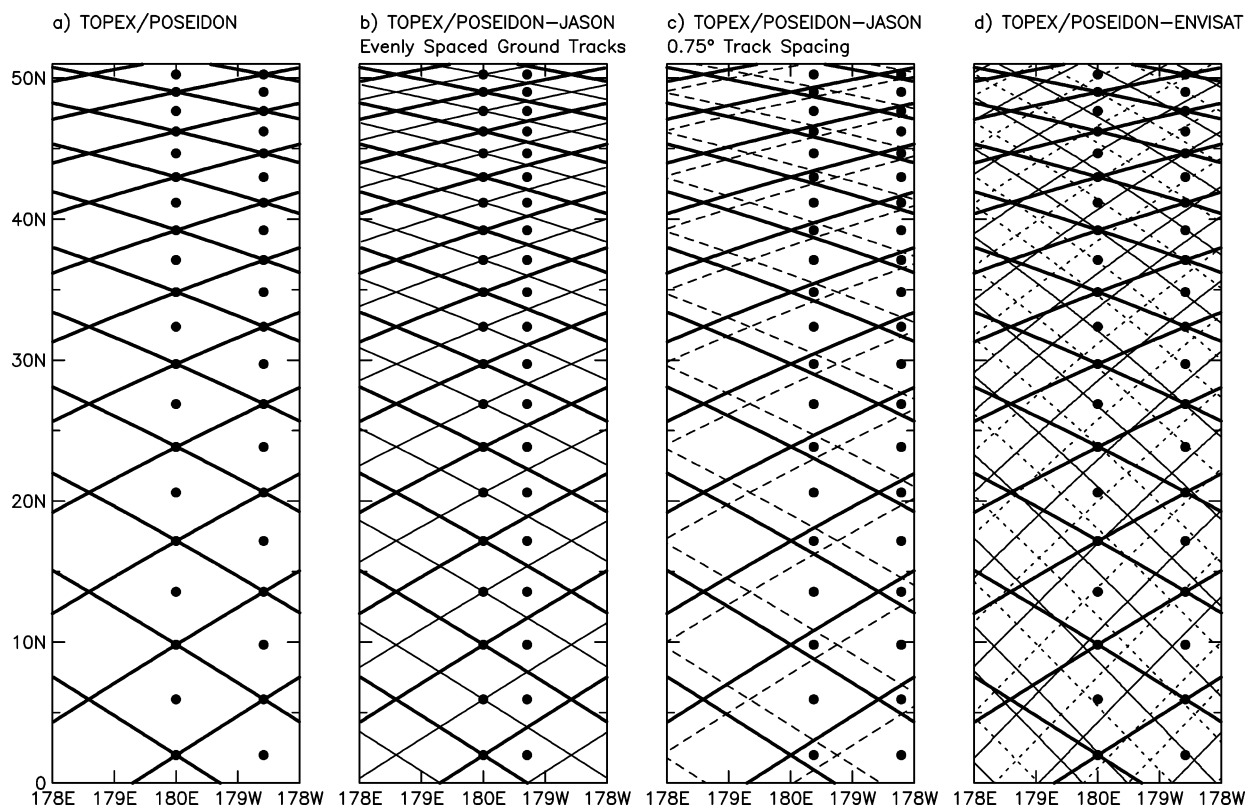
FIG. 4. The spatial sampling patterns in a longitudinal band near the international date line for (a) a single altimeter in the T/P orbit; (b) a tandem T/P and *Jason* sampling pattern with evenly spaced interleaved ground tracks; (c) a tandem T/P and *Jason* sampling pattern with ground tracks offset by 0.75°; and (d) a tandem *Jason* and *ENVISAT* sampling pattern. Heavy solid lines in all four panels correspond to the T/P ground tracks. The thin solid and dashed lines in (b) and (c) correspond, respectively, to the ground tracks of the evenly spaced, interleaved sampling pattern and the 0.75° offset sampling pattern. The thin solid and dashed lines in (d) correspond to the *ENVISAT* ground tracks during the first and second halves of the 35-day orbit repeat period. The dots in each panel indicate the locations at which the mapping errors were calculated to obtain the average values and the 90% quantile ranges of variation of rmse in Figs. 5, 9, 11, and 13.

4 cm in the unsampled diamond centers. With the coarse 2.834° spacing of the T/P ground tracks, it is necessary to increase the spatial smoothing to at least 5° to reduce the mapping errors to less than 4 cm everywhere, as shown in the right panel of Fig. 3.

Note that the errors with 5° smoothing are slightly larger at the crossovers, rather than at the diamond centers as in the case of the smaller 3° spatial smoothing in the middle panel of Fig. 3. With 3° smoothing, there are very few observations within the radius of influence for estimates at the diamond centers, thus resulting in the largest mapping errors occuring at the diamond centers. With the larger radius of influence for 5° smoothing, estimates at a diamond center include observations from the entire perimeter of the diamond, albeit with no observations close to the diamond center. For estimates at the crossovers, the radius of influence with 5° smoothing includes nearby observations along the two ground tracks that form the crossover but the estimates of smoothed SSH are poorly constrained by observations to the north, south, east, and west of the estimation location. At latitudes equatorward of 30°, latitudinal sampling imposes a greater limitation than longitudinal

sampling because of the latitudinal elongation of the diamond patterns formed by the intersecting ground tracks. In the units of degrees used here to define the spatial smoothing parameters, the meridional spacing of the latitudes of crossovers for T/P and *Jason* is larger than the zonal spacing equatorward of 30° (see Fig. 4 of GCS97). The result of the geographical distribution of observations from which estimates of 5° smoothed SSH are constructed is zonal banding of the errors along crossover latitudes with slightly larger errors near the crossovers. This geographical inhomogeneity diminishes poleward of 30° latitude where the spacing of the latitudes of crossovers becomes smaller than the longitudinal spacing between crossover points.

The lower meridional resolution that is responsible for the zonal banding of the tropical and midlatitude mapping errors in SSH fields constructed from altimeter sampling patterns has been quantified by Tai (1998). From consideration of SSH at the midpoints along the ground tracks between crossovers, he showed that the Nyquist aliasing wavelengths in the meridional and zonal directions are, respectively, the meridional and zonal dimensions of the diamonds formed by intersecting
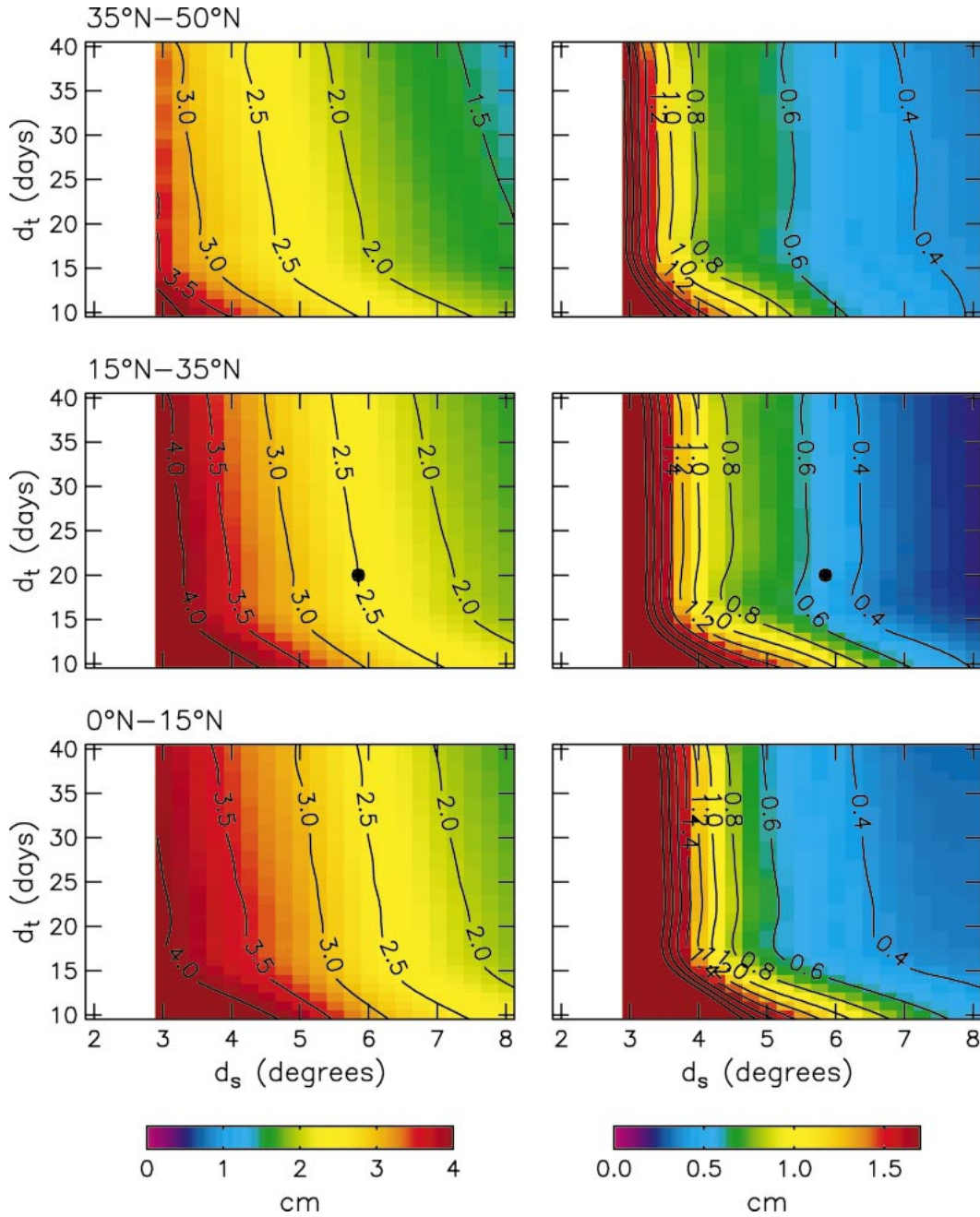
FIG. 5. (left) The averages and (right) 90% quantile ranges of variation of the rmse for SSH fields constructed from a single altimeter in the T/P orbit with spatial and temporal smoothing parameters d_s and d_t for (top) subpolar latitudes (35°–50°N), (middle) subtropical latitudes (15°–35°N), and (bottom) tropical latitudes (the equator to 15°N). The dots in the middle panels indicate the resolution capability in the subtropical band according to the criteria discussed in the text. Results are not shown for d_s less than 3° because the coarse 2.834° ground track spacing of the T/P sampling pattern is unable to resolve such short scales. For clarity, the maximum contour displayed in the plots of 90% quantile range of variation is 2 cm.

ground tracks. At 30° latitude, for example, the meridional aliasing wavelength deduced by Tai (1998) is about double that of the zonal aliasing wavelength.

In addition to the latitudinal banding equatorward of 30°N, a significant latitudinal variation of the mapping

errors is apparent from Fig. 3. For any particular choice of smoothing parameters, the errors are maximum near 20° latitude, decrease poleward of about 40° owing to the greater sampling density from the convergence of ground tracks, and decrease equatorward because of the
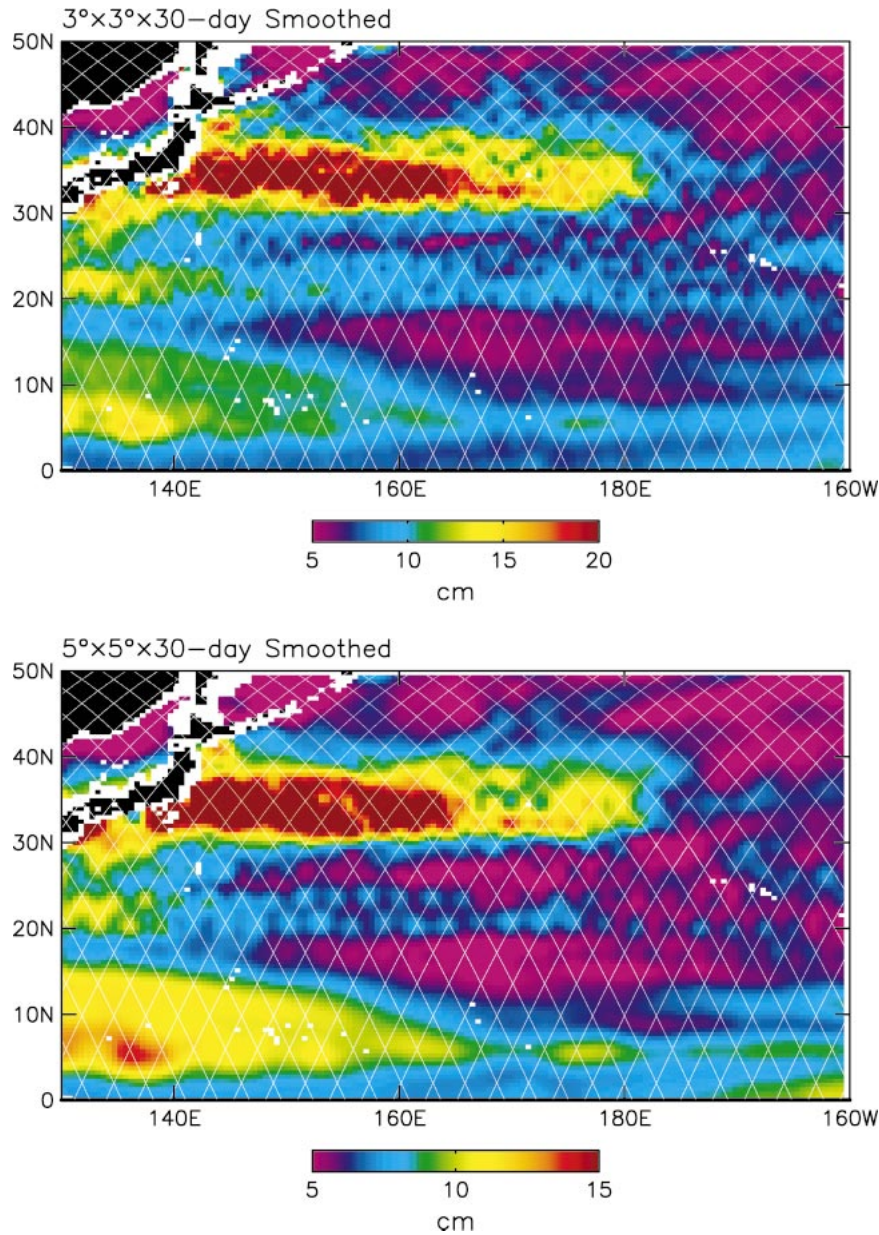
FIG. 6. The standard deviation of loess smoothed SSH fields computed from 7 yr of T/P data in the western North Pacific with (top) 3° × 3° × 30-day smoothing and (bottom) 5° × 5° × 30-day smoothing. Note the different color bars in the two figures.

increased spatial decorrelation scale (Fig. 2). The latitudinal variation of the relatively higher errors at intermediate latitudes represents a trade-off between the increase in the local sampling density with increasing latitude and the decrease in the spatial decorrelation scale with increasing latitude.

To investigate the effects of smoothing on the accuracy of SSH fields in more detail, the rmse were computed for wide range of spatial and temporal smoothing parameters at the 40 representative locations shown in Fig. 4a at daily intervals over the 10-day repeat period

(a total of 400 estimation times and locations). Because of the variation of mapping errors with latitude, the error characteristics are summarized in Fig. 5 for three different latitude bands: a subpolar band from 35° to 50°N (top panels), a subtropical band from 15° to 35°N (middle panels), and a tropical band from the equator to 15°N (bottom panels). The means and 90% quantile ranges of the T/P mapping errors over the estimation times and locations within each latitude band are shown for quadratic loess smoothing parameters corresponding to isotropic spatial filter cutoffs d_s ranging from 3° to 8° and
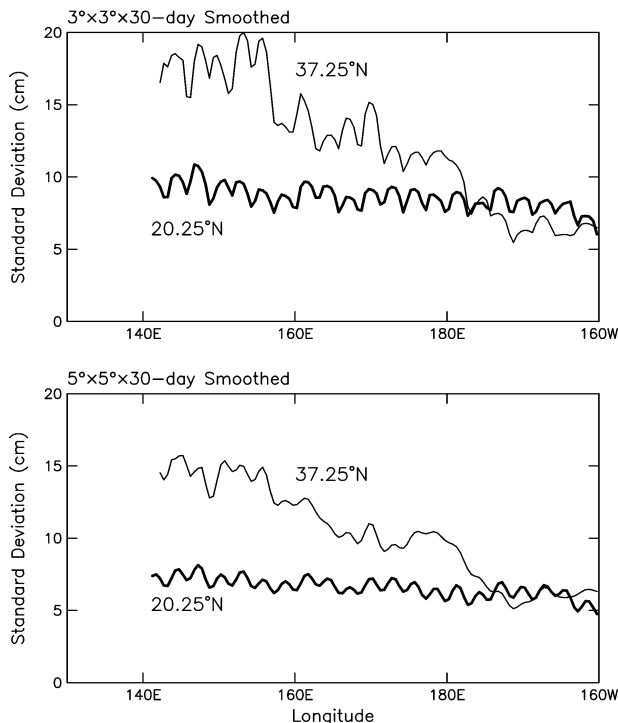
FIG. 7. Longitudinal profiles along 37.25°N (thin lines) and 20.25°N (heavy lines) from the maps of the standard deviation of loess smoothed SSH in Fig. 6.

temporal filter cutoffs d_t ranging from 10 to 40 days. It is evident that the mean mapping errors within each latitude band for any particular combination of d_s and d_t are about 20% smaller in the subpolar band than in the subtropical and tropical latitude bands.

Except for temporal smoothing shorter than about 20 days, it is apparent from Fig. 5 that the mean and 90% quantile range of variation of rmse for a given degree of spatial smoothing depend only weakly on the degree of temporal smoothing; increasing the temporal smoothing for a given degree of spatial smoothing has little effect on the accuracy of the SSH fields. The mapping errors for a single altimeter in the T/P orbit are more sensitive to spatial smoothing. For high-resolution mapping of the SSH field, the coarse 2.834° longitudinal spacing of the T/P ground tracks is therefore more limiting than the 10-day orbit repeat period.

Based on the 2.5-cm threshold for the mean rmse suggested in section 2, the filter cutoff wavelength and period defining the resolution capability of the T/P sampling pattern in the subtropical band is about 6° by 20 days. The 90% quantile range of variation of rmse for this smoothing is about 0.5 cm, which falls well within the 1.0-cm criterion adopted here. The mean and 90% quantile range of variation of rmse begin to increase rapidly if the temporal smoothing is reduced to less than about 20 days or the spatial smoothing is reduced to less than about 5.0°.

Our assessment of $6° \times 6° \times 20$ days for the reso-

lution capability of the T/P sampling pattern is quite comparable to the $3° \times 6° \times 20$-day resolution deduced by Tai (1998). The greater degree of zonal smoothing required here is due in part to the more stringent requirement of reducing the mean mapping errors to the threshold of 2.5 cm on the fine spatial grid considered here (and used in most applications of altimeter data). The aliasing considerations of Tai (1998) are specific to estimates at only the midpoints along the ground tracks halfway between each crossover. Moreover, the method of Tai (1998) does not explicitly treat the effects of measurement errors, of which the orbit errors are most problematic. The threshold of 2.5 cm for the mean mapping error adopted here imposes additional constraints beyond the effects of unresolved variability considered by Tai (1998), thus requiring a somewhat greater degree of smoothing than would be required to address only the aliasing limitations.

The 6° by 20-day resolution capability of the T/P sampling pattern is perhaps surprisingly coarse. As shown previously in Fig. 1, these filter cutoffs are analogous to the filtering properties of block averages with dimensions of about 3.6° by 12 days and are essentially the same as the 6° by 25-day smoothing recommended by GCS97. The need for such heavy spatial smoothing is illustrated in Fig. 6. The top panel shows the standard deviation of 3° by 30-day loess-smoothed estimates of SSH on a 0.5° grid at 10-day intervals constructed from 7 yr of T/P data. Within the latitude range from about 15° to 40°N, the standard deviation is systematically lower at the diamond centers than at the neighboring crossovers to the east or west, creating a sampling-induced zonally periodic pattern. The zonal periodicities are shown more clearly for two selected latitudes in the top panel of Fig. 7.

The geographical pattern in the standard deviation of the 3° spatially smoothed SSH in the top panels of Figs. 6 and 7 is directly related to the geographical pattern in the rmse (see the middle panel of Fig. 3). The spatial inhomogeneities of the mapping errors and of the standard deviation of the smoothed SSH fields are much smaller poleward of 40° and are somewhat smaller equatorward of 10°.

Patchiness from sampling errors is also apparent in the standard deviation of 5° by 30-day smoothed SSH fields shown in the bottom panel of Fig. 6. Locally larger variability at the crossovers is most notable near 35°N within the zonal band of energetic variability associated with the Kuroshio Extension. The effects of sampling errors are also apparent between 20°N and 25°N, though more difficult to discern because of the smaller overall amplitude of the SSH variability within this latitude band. Sampling-induced zonal periodicities with 5° smoothing are shown more clearly in the lower panel of Fig. 7 for two selected latitudes. The patchiness in the standard deviation is directly related to the geographical pattern in the rmse for 5° spatial smoothing (see the right panel of Fig. 3). It is clear that 5° spatial
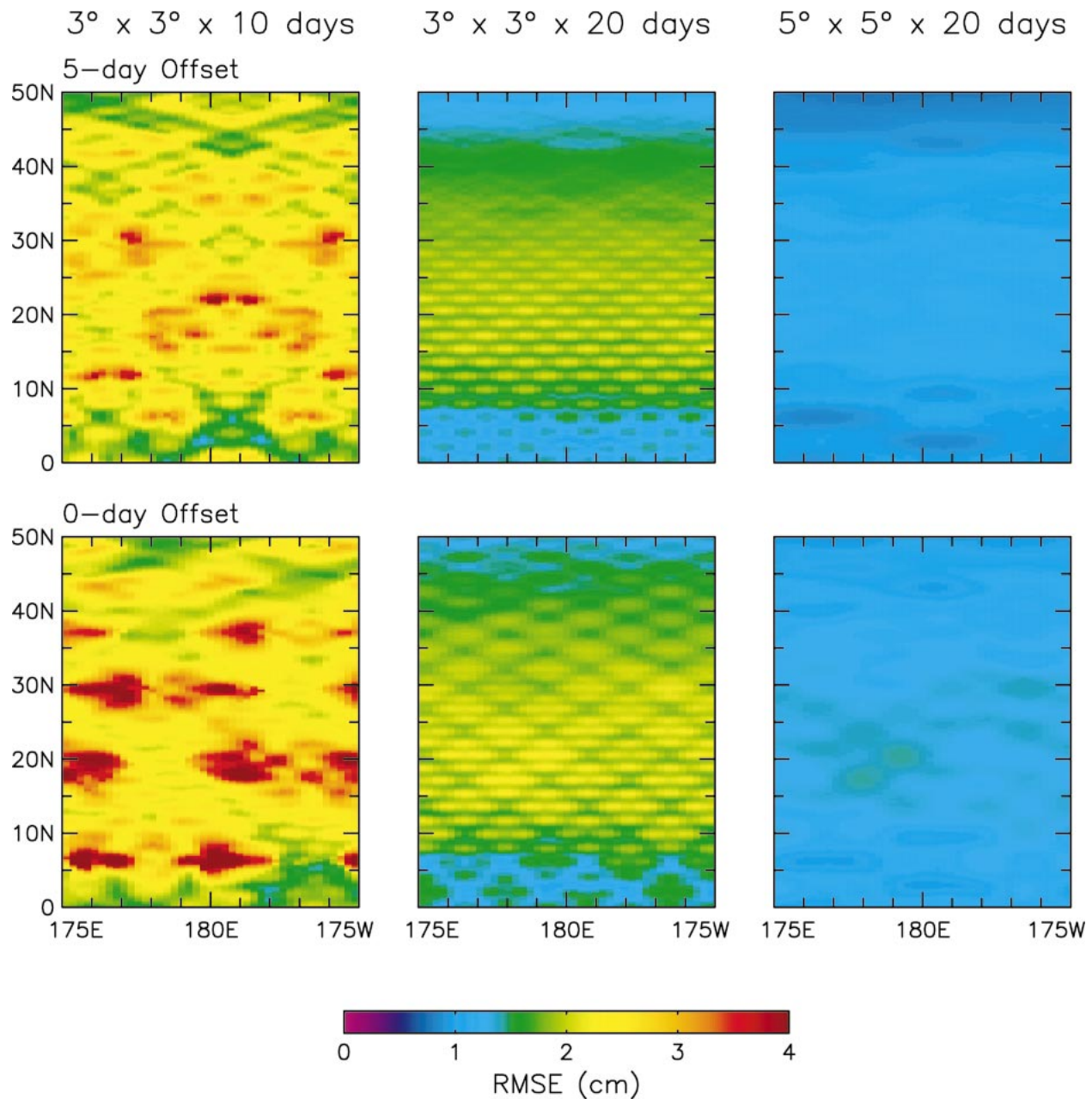
FIG. 8. As in Fig. 3 except for SSH fields constructed from measurements from a tandem T/P–*Jason* sampling pattern with evenly spaced, interleaved ground tracks. The panels correspond to (top) 5-day and (bottom) 0-day offsets between neighboring T/P and *Jason* ground tracks.

smoothing is not sufficient to suppress geographical in- homogeneity of mapping errors from poorly resolved mesoscale variability.

b. A tandem T/P–Jason sampling pattern with evenly spaced ground tracks

The rmse presented here for a tandem T/P–*Jason* mis- sion are based on values of $\sigma_e = 2$ cm and $\sigma_o = 2$ cm for both altimeters. Maps of rmse for SSH fields con-

structed from interleaved tandem T/P–*Jason* sampling patterns with evenly spaced ground tracks separated by 1.417° of longitude are shown in Fig. 8 for three choices of smoothing parameters and two choices of the time offset between the parallel T/P and *Jason* ground tracks. The upper and lower panels show, respectively, the map- ping errors for 5-day and 0-day offsets between parallel ground tracks of T/P and *Jason*. The 7-min time offset between neighboring ground tracks that was adopted for the tandem T/P–*Jason* mission that began on 16 Sep-

tember 2002 is equivalent to what is referred to here as the 0-day offset. The two choices of time offset are considered here to determine whether either offers a significant advantage over the other.

The rmse for both of these interleaved tandem T/P–*Jason* orbits decrease by almost a factor of 2 compared with the mapping errors in Fig. 3. For the case of the 3° by 10-day smoothing shown in the left panels of Fig. 8, there are patches of errors in excess of 4 cm. These patches are larger in geographical extent for the 0-day offset than for the 5-day offset, indicating a preference for the 5-day offset for this small degree of smoothing. The precise locations of the patches of large errors for the 0-day offset migrate around the map for different estimation times during the 10-day repeat cycle. When the temporal smoothing is increased to 20 days, the localized patches of large mapping errors are eliminated and the mapping errors are essentially indistinguishable for these two tandem sampling patterns.

The means and 90% quantile ranges of the mapping errors for the 5-day offset interleaved sampling pattern are shown in Fig. 9a as functions of spatial and temporal smoothing parameters. The mapping errors were computed at the 40 locations shown in Fig. 4b and at daily intervals over the 10-day repeat period. It is evident from comparisons of the left panels of Figs. 5 and 9a that the mean mapping errors from the interleaved tandem orbit are more than a factor of 2 smaller than for the case of the single altimeter considered in section 3a. For small spatial filtering, the 90% quantile ranges of variation of the rmse in Fig. 9a decrease by a factor of about 7 in the subtropical latitude band and by a factor of 3 or 4 in the subpolar and tropical bands, compared with the rmse for the single altimeter (Fig. 5).

For the mean error threshold of 2.5 cm, the resolution capability in the subtropical band is about 2.2° by 20 days for this interleaved tandem orbit. The corresponding 90% quantile range of variation of rmse is about 0.2 cm, well within the threshold criterion of 1.0 cm adopted here. The spatial resolution of 2.2° is nearly a factor-of-3 improvement over the 6° spatial resolution capability of a single altimeter in the T/P orbit. For the mean error threshold adopted here and 20-day temporal smoothing, the spatial smoothing could be decreased to less than 2° in the subpolar band without violating the 1-cm threshold for the variability. In the tropical band, the 90% quantile range of variability exceeds 1 cm for $d_s < 2°$.

Differences between the averages and 90% quantiles of mapping errors for the interleaved sampling patterns with 0-day or 5-day offsets are mostly minor except in the tropical latitude band when the smoothing parameters are shorter than 3° spatially and/or 20 days temporally (Fig. 9b). While the mean rmse in the Tropics is only slightly larger for the 0-day offset (compare the bottom-left panels of Figs. 9a and 9b), the spatial and temporal inhomogeneity of the rmse exceeds the 1-cm threshold criterion for d_s smaller than about 3° or for d_t

smaller than about 15 days (compare the bottom-right panels of Figs. 9a and 9b). The mapping errors for the 0-day offset are also much more inhomogeneous at subtropical latitudes for d_t smaller than about 15 days (compare the middle-right panels of Figs. 9a and 9b; see also the left panels of Fig. 8). For such small smoothing, the 5-day offset yields better estimates of smoothed SSH than can be obtained from the 0-day offset adopted for the present tandem T/P–*Jason* mission.

c. A tandem T/P–Jason sampling pattern with 0.75° track spacing

Maps of rmse for the tandem T/P–*Jason* sampling pattern with 0.75° track separation and 0-day offset are shown in Fig. 10 for the same three choices of smoothing parameters considered in Figs. 3 and 8. While this tandem sampling pattern yields SSH fields with mapping errors smaller than those from T/P alone (Fig. 3), the improvement is modest compared with that obtained for the evenly spaced, interleaved sampling patterns considered in Fig. 8. The closer 0.75° spacing of the parallel T/P and *Jason* ground tracks leaves large diamond-shaped regions unsampled [see Fig. 4(c)]. For 3° by 10-day smoothing, there are large areas with mapping errors exceeding 4 cm. Errors larger than 4 cm still exist when the temporal smoothing is increased to 20 days. When the smoothing is increased to 5°, the mapping errors for the 0.75° offset tandem orbit decrease to less than 3 cm everywhere, but this is about a factor of 2 larger than the mapping errors from the evenly spaced, interleaved ground track pattern with the same 5° by 20-day smoothing.

The mean values and 90% quantile ranges of variation of rmse for a 0.75° offset tandem T/P–*Jason* sampling pattern are shown in Fig. 11 as functions of spatial and temporal smoothing parameters. The mapping errors were computed at the 40 locations shown in Fig. 4c and at daily intervals over the 10-day repeat period. For the mean error threshold of 2.5 cm, the resolution capability of SSH fields constructed from the 0.75° offset tandem orbit is about 3.7° by 20 days in the subtropical band. The corresponding 90% quantile range is about 0.8 cm, which is less than the threshold criterion of 1.0 cm. With 20-day temporal smoothing, the spatial smoothing could be reduced to about 2.7° within the subpolar band. With a 1-cm threshold for the 90% quantile range of variability, the spatial resolution capability for 20-day temporal smoothing in the tropical band is no better than the 3.7° resolution capability within the subtropical band.

d. The tandem Jason–ENVISAT sampling pattern

The European Space Agency launched the *ENVISAT* satellite in March 2002 as a successor to the *ERS-1* and *ERS-2* satellites. *ENVISAT* was placed into the same orbit as the ERS satellites with a 98° inclination and a
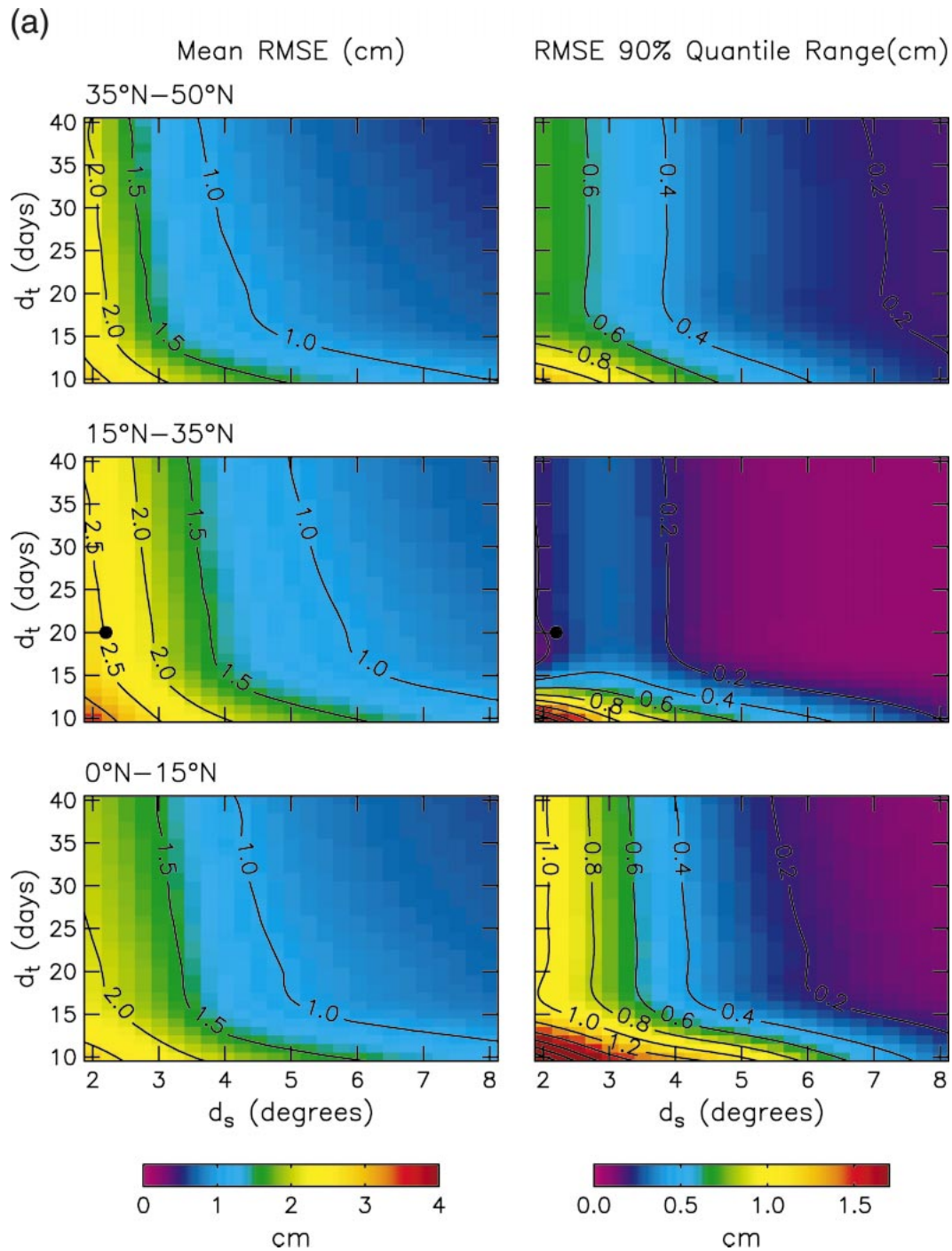
FIG. 9a. As in Fig. 5 except for SSH fields constructed from measurements from a tandem T/P–*Jason* sampling pattern with evenly spaced ground tracks with 5-day offset. The averages and 90% quantile ranges were computed from estimates at the 40 locations shown in Fig. 5b and at daily intervals over the 10-day repeat cycle.

35-day exact repeat. Since *ENVISAT* is operating simultaneously with *Jason,* it is useful to explore the possibility of obtaining high-resolution SSH fields from this tandem altimeter dataset. This exercise is complicated by the lack of coordination of the two orbit configurations (the different repeat periods and different orbit inclinations) and the fact that the orbit errors are expected to be larger by a factor of 2 or more for *ENVISAT* than for *Jason.*

Maps of rmse for the tandem *Jason–ENVISAT* sampling pattern are shown in Fig. 12 for the three choices of smoothing parameters considered previously. For the
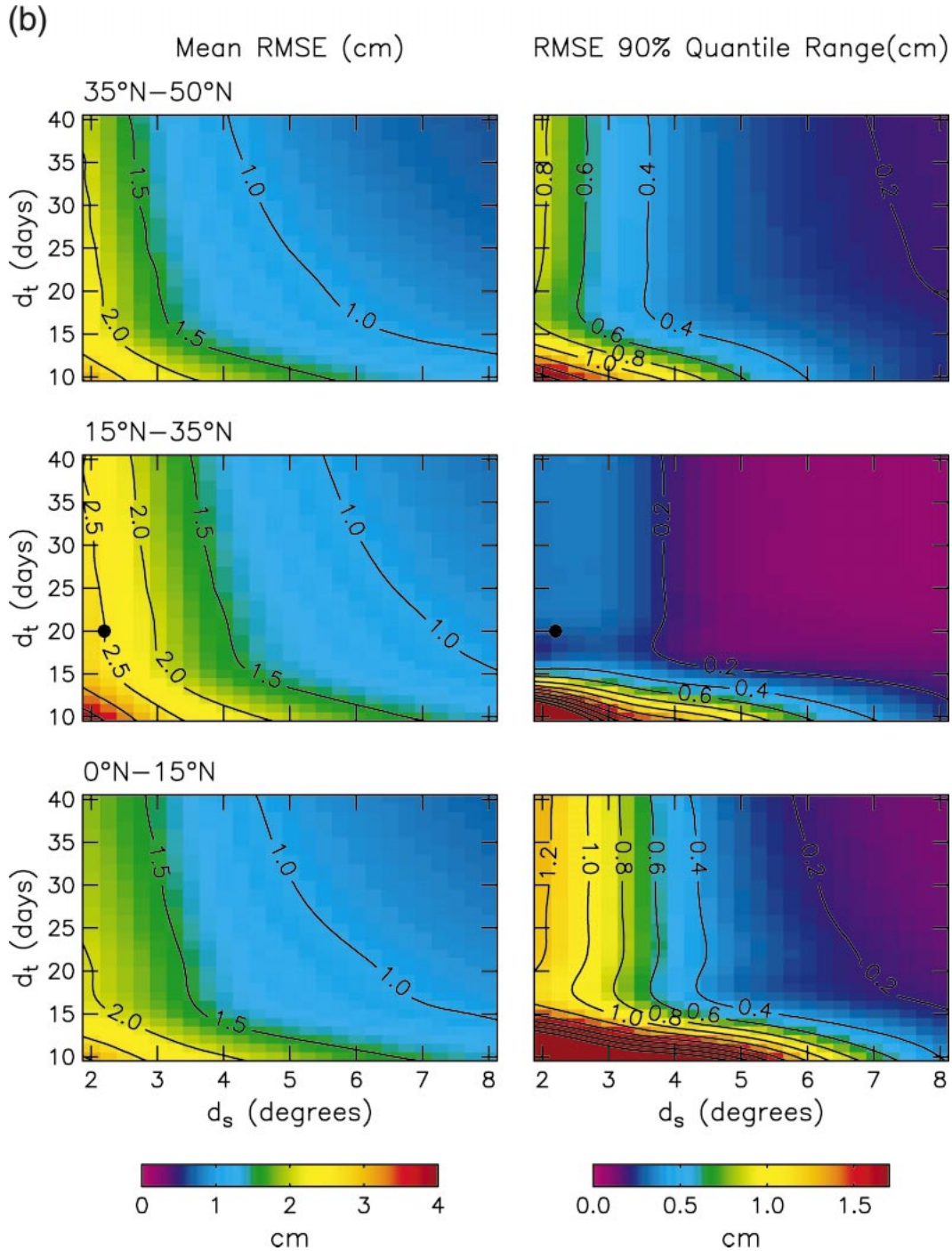
FIG. 9b. As in Fig. 9a except for the case of evenly spaced ground tracks with 0-day offset.

upper panels, the *ENVISAT* orbit errors have been assumed to have a standard deviation of 4 cm. As in sections 3b and 3c, the *Jason* orbit errors are assumed to have a standard deviation of 2 cm. For 3° by 10-day smoothing (top left panel of Fig. 12), the patches of elevated rmse are both larger in magnitude and more extensive geographically than for the case of the inter-

leaved, evenly spaced tandem T/P–*Jason* sampling pattern with either the 0-day or 5-day offset. These patches of large mapping errors migrate geographically for different estimation times in response to the complicated space–time sampling of the combined 35-day *ENVISAT* and 10-day *Jason* ground track patterns.

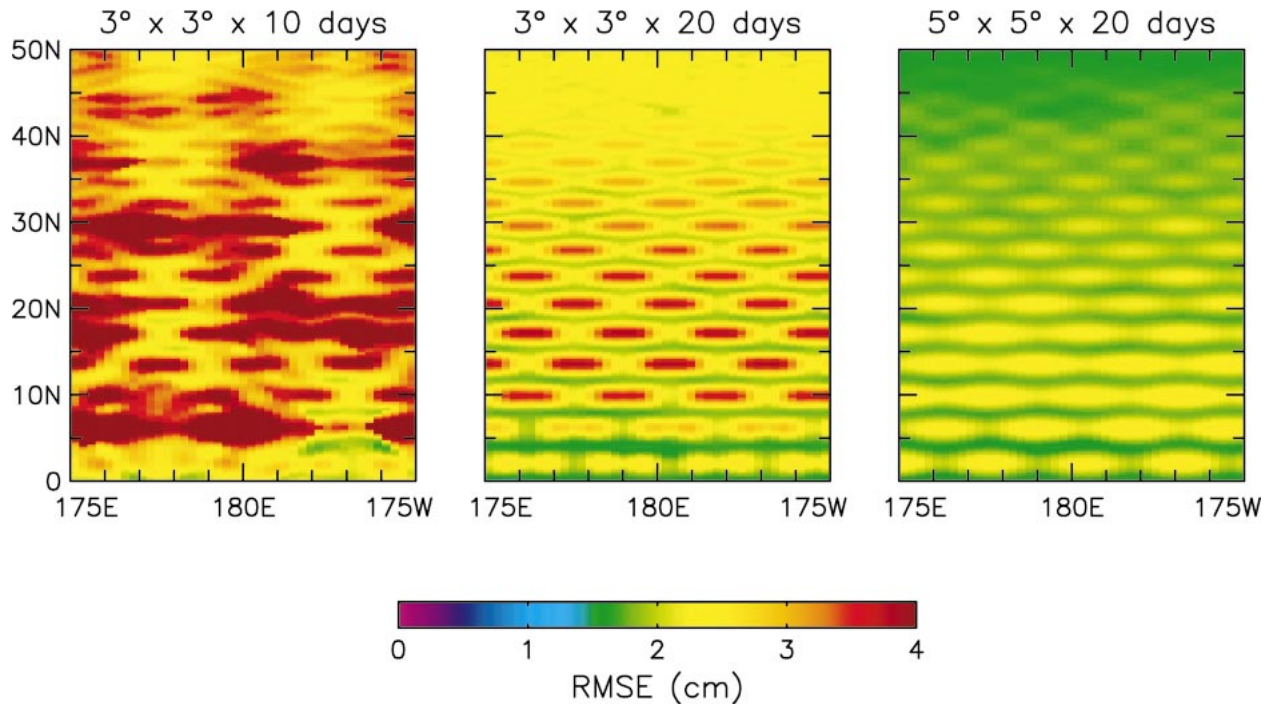When the smoothing is increased to 3° by 20 days

FIG. 10. As in Figs. 3 and 8 except for SSH fields constructed from measurements from a tandem T/P–*Jason* sampling pattern with 0.75° offset between the parallel T/P and *Jason* ground tracks.

(top-middle panel of Fig. 12), the *Jason–ENVISAT* mapping errors are reduced considerably, but are still inhomogeneous, ranging from a low of about 1.5 cm to a high of about 3.5 cm. In comparison, the tandem T/P–*Jason* sampling pattern with evenly spaced ground tracks yields mapping errors for 3° by 20-day smoothing that are nearly homogeneous with a value of about 2 cm in the subtropical band (middle panels of Fig. 8). Increasing the spatial smoothing of tandem *Jason–ENVISAT* data to 5° (top-right panel of Fig. 12) reduces the mapping errors to less than 2.5 cm everywhere, compared with maximum mapping errors of about 1.25 and 1.5 cm for the T/P–*Jason* sampling patterns with 5-day and 0-day offsets, respectively.

The mean value and the 90% quantile range of variation of the rmse for a tandem *Jason–ENVISAT* sampling pattern with *ENVISAT* orbit errors of 4 cm are shown in Fig. 13a as functions of spatial and temporal smoothing parameters. The mapping errors were computed at the 40 locations shown in Fig. 4d and at daily intervals over the 35-day *ENVISAT* repeat period, that is, at a total of 1400 estimation times and locations. The structures of these rmse plots are notably different from the rmse plots considered previously for the single and tandem T/P and *Jason* sampling patterns. For a given degree of spatial smoothing d_s, increasing the temporal smoothing d_t is more effective at reducing the mapping errors from the tandem *Jason–ENVISAT* data. This is because the close spacing of the *ENVISAT* ground tracks reduces the spatial resolution limitation that is inherent

in the T/P and *Jason* sampling patterns, thus elevating the relative importance of the temporal resolution limitation of the long 35-day orbit repeat period.

In comparison with the results for the interleaved tandem T/P–*Jason* sampling pattern with evenly spaced ground tracks and 5-day offset (Fig. 9a), the 90% quantile ranges in Fig. 13a are at least a factor of 2 larger for small amounts of smoothing. This is a quantitative measure of the greater inhomogeneity of rmse noted above from the example error maps in Fig. 12. The migration of the inhomogeneous mapping errors in space and time that is responsible for these larger 90% quantile ranges would contaminate wavenumber-frequency spectra of SSH variability in a very complicated manner. The energy level of these artifacts in SSH fields constructed from a tandem *Jason–ENVISAT* sampling pattern might obscure the spectral characteristics of SSH signals that are of interest (e.g., the Rossby wave dispersion application discussed below in section 4a).

By the threshold mean error criterion of 2.5 cm, it is evident from Fig. 13a that the resolution capability of the tandem *Jason–ENVISAT* sampling pattern for *ENVISAT* orbit errors of 4 cm is about 3° by 20 days in the subtropical latitude band. The corresponding 90% quantile range is about 0.8 cm, which is within the tolerance criterion of 1.0 cm but is a factor of 4 larger than the 90% quantile range for the tandem T/P–*Jason* case with evenly spaced ground tracks and 5-day offset. This reflects the much greater spatial and temporal inhomogeneity of mapping errors noted in Fig. 12. The
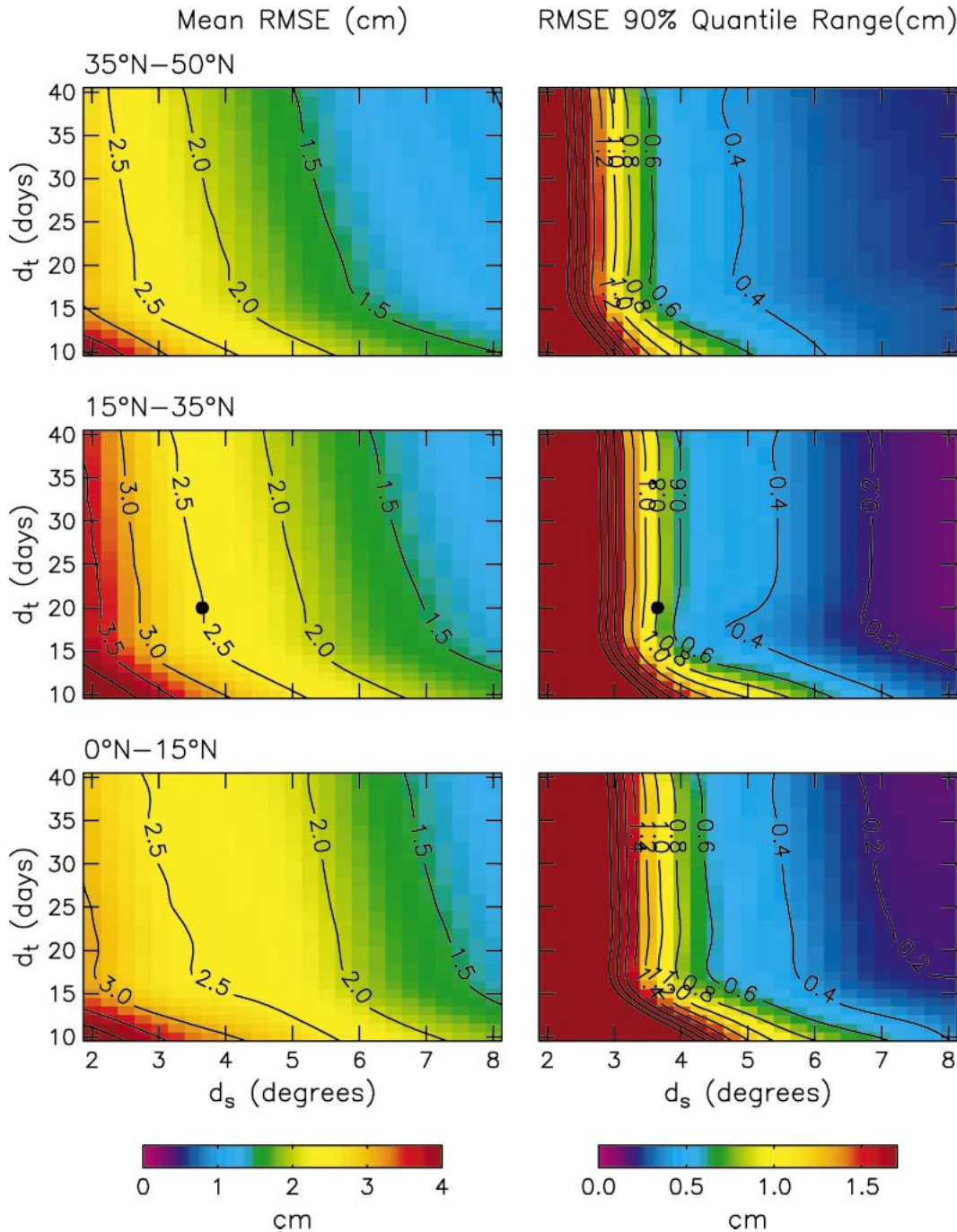
FIG. 11. As in Figs. 5 and 9 except for SSH fields constructed from measurements from a tandem T/P–*Jason* sampling pattern with 0.75° offset between the parallel ground tracks. The averages and 90% quantile ranges were computed from estimates at the 40 locations shown in Fig. 4c and at daily intervals over the 10-day repeat cycle.

spatial resolution capability of 3° is a significant improvement over the 3.7° resolution capability of the tandem T/P–*Jason* mission with 0.75° spacing of simultaneously sampled parallel ground tracks. For 20-day smoothing, the spatial resolution capability of the tandem *Jason–ENVISAT* sampling pattern improves to about 2.5° in the subpolar and tropical bands.

It is noteworthy that the 3° resolution capability deduced here for the tandem *Jason–ENVISAT* sampling pattern is better by more than a factor of 2 than the resolution capability deduced by GCS97 for the equivalent tandem T/P–ERS sampling pattern. In part, this is because of the longer signal decorrelation scale adopted here (Fig. 2). Another factor is that the computational
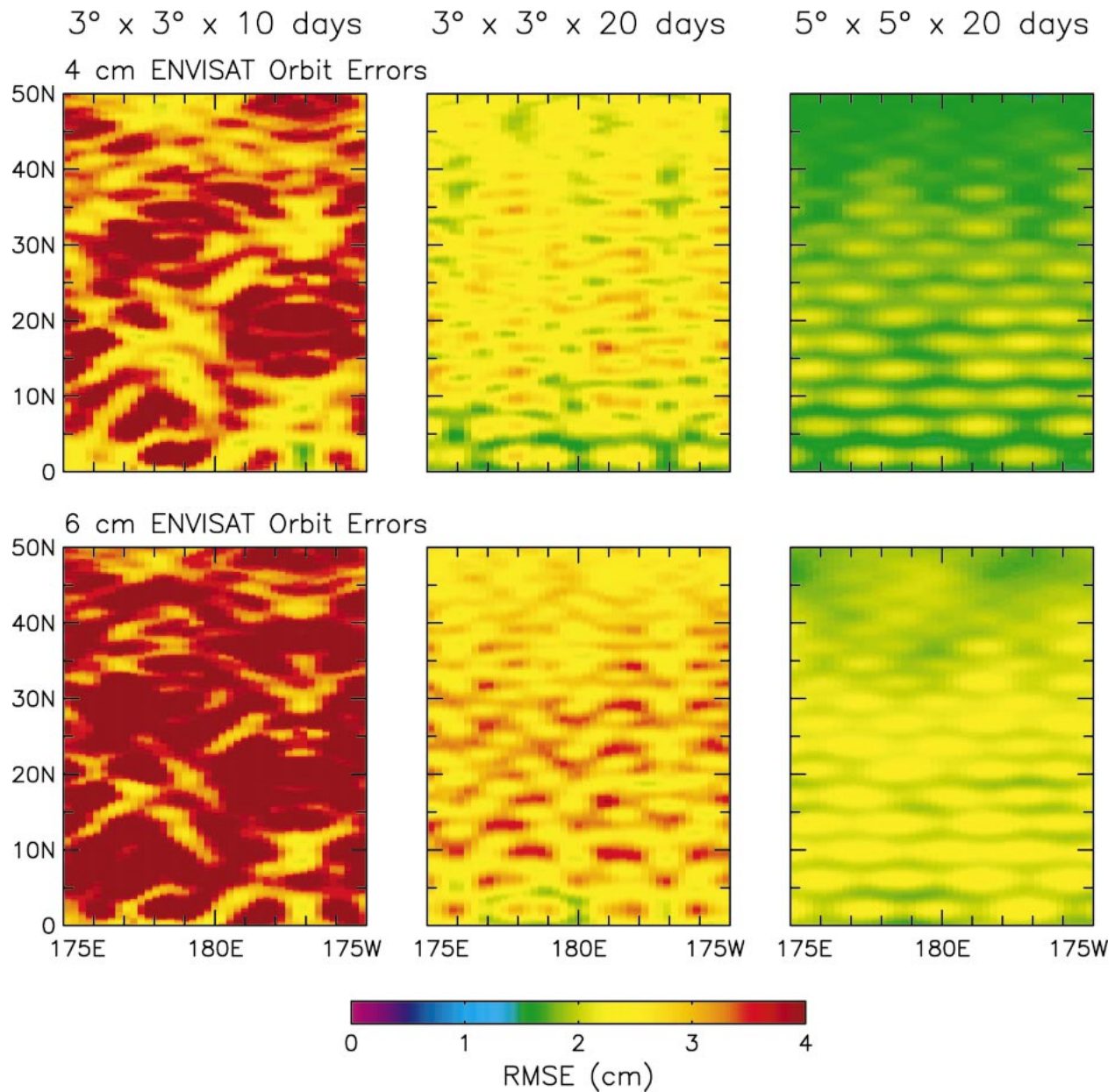
FIG. 12. As in Figs. 3, 8, and 10 except for SSH fields constructed from measurements from a tandem *Jason–ENVISAT* sampling pattern. Mapping errors for the cases of *ENVISAT* orbit errors with standard deviations of (top) 4 cm and (bottom) 6 cm, respectively. The *Jason* orbit errors are assumed to have a standard deviation of 2 cm in all of these simulations.

demands of the method used by GCS97 restricted the calculation of the mapping errors to only two locations (see Fig. 7 of GCS97), which may not have adequately represented the mapping errors over a large geographical domain. Probably most significantly, the maximum deviation from the mean mapping error considered by GCS97 is more demanding than the 90% quantile measure of spatial and temporal inhomogeneity of mapping errors used here, as noted previously in section 2. Because of the long-tailed nature of the rmse distribution for the tandem *Jason–ENVISAT* sampling pattern (i.e.,

occasional extreme values of mapping errors geographically at a specific estimation time or temporally at a given estimation location), the maximum deviation is much larger than the 90% quantile range of rmse. This leads to the more conservative estimate of resolution capability suggested by GCS97. Maps and time series of smoothed SSH constructed from tandem *Jason–ENVISAT* data with the 3° spatial smoothing suggested here will thus be contaminated by occasional large outliers owing to sampling errors [see Figs. 2 and 3 of Greenslade et al. (1997)].

Since there is some uncertainty about how accurately the orbits can be estimated for *ENVISAT,* it is useful to investigate the sensitivity of the mapping errors to the magnitude of the orbit errors. The SSH mapping errors for the case of *ENVISAT* orbit errors with a larger standard deviation of 6 cm are shown in the bottom panels of Fig. 12 for the three choices of smoothing parameters considered previously. The mapping errors are larger by 25%–50% than for the case of *ENVISAT* orbit errors with a standard deviation of 4 cm (top panels of Fig. 12). These increases are typical of the increases of the average values of the rmse over the full range of smoothing parameters (Fig. 13b). Moreover, the 90% quantile ranges are also considerably larger with 6-cm orbit errors for SSH fields constructed with small spatial smoothing. If *ENVISAT* were to have orbit errors this large, the resolution capability of SSH fields constructed from the tandem *Jason–ENVISAT* sampling pattern according to the same criteria adopted previously would be degraded to about 4° by 20 days in the Tropics and subtropics, and to about 3.25° by 20 days in the subpolar latitude band.

e. Summary

The resolution capability of SSH fields constructed from the various altimeter sampling patterns considered above has been assessed from the mean and 90% quantile range of variation of the mapping errors based on an assumed signal standard deviation of 10 cm. When multiplied by 10, the threshold values of 2.5 and 1.0 cm adopted here for the mean and 90% quantile range can be interpreted as the percentages of signal standard deviation. The results presented here are thus easily extended to the case of arbitrary signal standard deviation. The threshold criteria for the average value and the 90% quantile range of variation of rmse correspond, respectively, to 25% and 10% of the SSH signal standard deviation. The wavenumber-frequency distribution of the signal variance is specified by the Gaussian form assumed here for the space–time autocorrelation of SSH. The metric used here to assess the mapping errors is based on the mean-squared difference between the quadratic loess estimate and the best possible estimate of smoothed SSH that would be obtained by the quadratic loess smoother if the observations were continuously distributed in space and time.

In order to reduce the number of parameters under consideration, the focus here has been on the root-mean-squared errors of SSH fields constructed from measurements from various altimeter sampling patterns based on temporal smoothing with a filter cutoff period of 20 days, which corresponds approximately to the filtering properties of 12-day block averages and is thus commensurate with the 10-day repeat period of the T/P and *Jason* orbits. The spatial resolutions differ considerably for the various sampling patterns. As a baseline for comparison, it was shown in section 3a that SSH can be mapped from measurements from a single altimeter in the T/P orbit with a spatial resolution defined by a filter cutoff wavelength of about 6°. This corresponds approximately to the filtering properties of 3.6° block averages.

Tai (1998) deduced a similar midlatitude resolution limitation of 3° of longitude by 6° of latitude by 20 days from a consideration of the harmonics that can be resolved in least squares fits using SSH at the midpoints along the satellite ground tracks halfway between crossovers. The somewhat greater zonal smoothing suggested here mitigates the effects of measurement and orbit errors that were not explicitly treated by Tai (1998) and reduces the spatial inhomogeneity of the mapping errors to a level at which SSH fields can be constructed with acceptably small mean rmse on a much finer spatial grid than just the midpoints.

Of the tandem T/P–*Jason* missions considered here, the sampling patterns with evenly spaced ground tracks considered in section 3b are the best for mapping the SSH field. The 5-day offset between parallel tracks is preferable to the 0-day offset, especially in the tropical band where the spatial and temporal inhomogeneity of mapping errors with small smoothing is considerably larger for the 0-day offset. In the subtropical band, the resolution capability of both evenly spaced ground track sampling patterns is about 2.2°, which is far superior to the 3.7° resolution capability of the tandem T/P–*Jason* sampling pattern with 0.75° ground track spacing considered in section 3c. Depending on the precise magnitudes of the *ENVISAT* orbit errors, even the uncoordinated tandem *Jason–ENVISAT* sampling pattern (see section 3d) yields SSH fields with spatial resolution better than that of the tandem T/P–*Jason* sampling pattern with 0.75° ground track spacing.

The relative accuracies of SSH maps constructed from the various altimeter sampling patterns considered in this study can be inferred from the average value and 90% quantile range of variation of rmse for each sampling pattern for a specific choice of smoothing parameters. The results for the case of smoothing with filter cutoff wavelength and period of 3° by 20 days are shown in Fig. 14. The various sampling patterns are displayed on the abscissa in order of decreasing average rmse. For the cases considered, the spatial and temporal inhomogeneities of the mapping errors as characterized by the 90% quantile range of variation decrease in rough proportion to the overall average mapping error.

The values of 25% and 10% of the SSH signal standard deviation adopted here as threshold values of the average value and the 90% quantile range of variation of rmse are admittedly ad hoc. They are based on our subjective judgment of the amount of smoothing required to obtain usefully accurate SSH fields from T/P data (see Figs. 6 and 7). The key point, however, is that a consistent set of criteria are used to evaluate the mapping resolution capabilities of all of the altimeter sampling patterns considered here. Our conclusions about the resolution capabilities of the various altimeter sam-
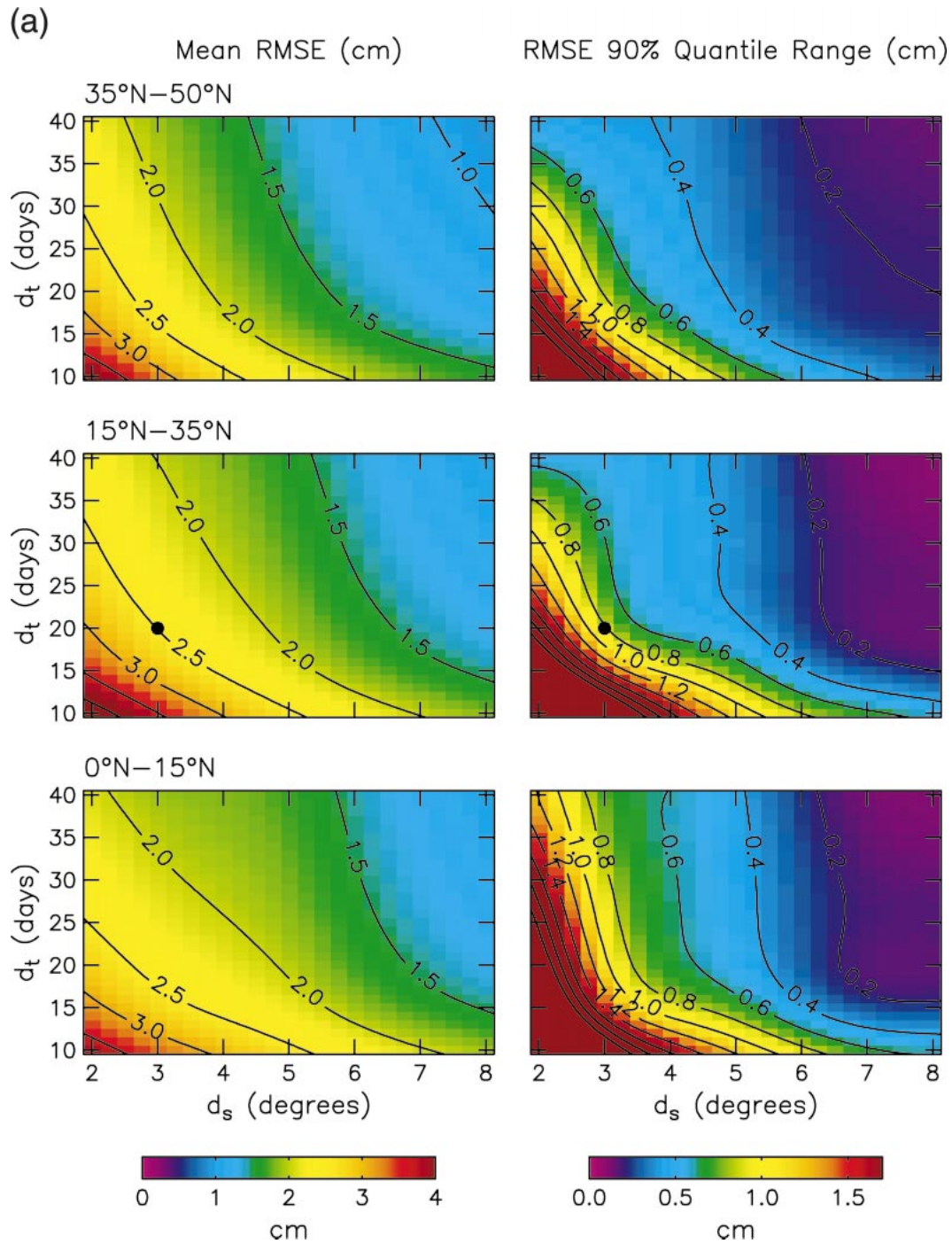
FIG. 13a. As in Figs. 5, 9, and 11 except for SSH fields constructed from measurements from a tandem *Jason–ENVISAT* sampling pattern with *ENVISAT* and *Jason* orbit errors with standard deviations of 4 and 2 cm, respectively. The averages and 90% quantile ranges were computed from estimates at the 40 locations shown in Fig. 4d and at daily intervals over the 35-day repeat cycle of the *ENVISAT* orbit configuration.

pling patterns are summarized in Fig. 15. If different threshold values for the average and 90% quantile ranges were adopted, the conclusions about the precise values of the spatial and temporal resolution capability would differ somewhat. However, the relative accura-

cies of the various sampling patterns would not likely differ much from what is shown in Figs. 14 and 15.

The threshold tolerance of 25% of the signal standard deviation for the average mapping error was sufficient to define the SSH mapping resolution capability for
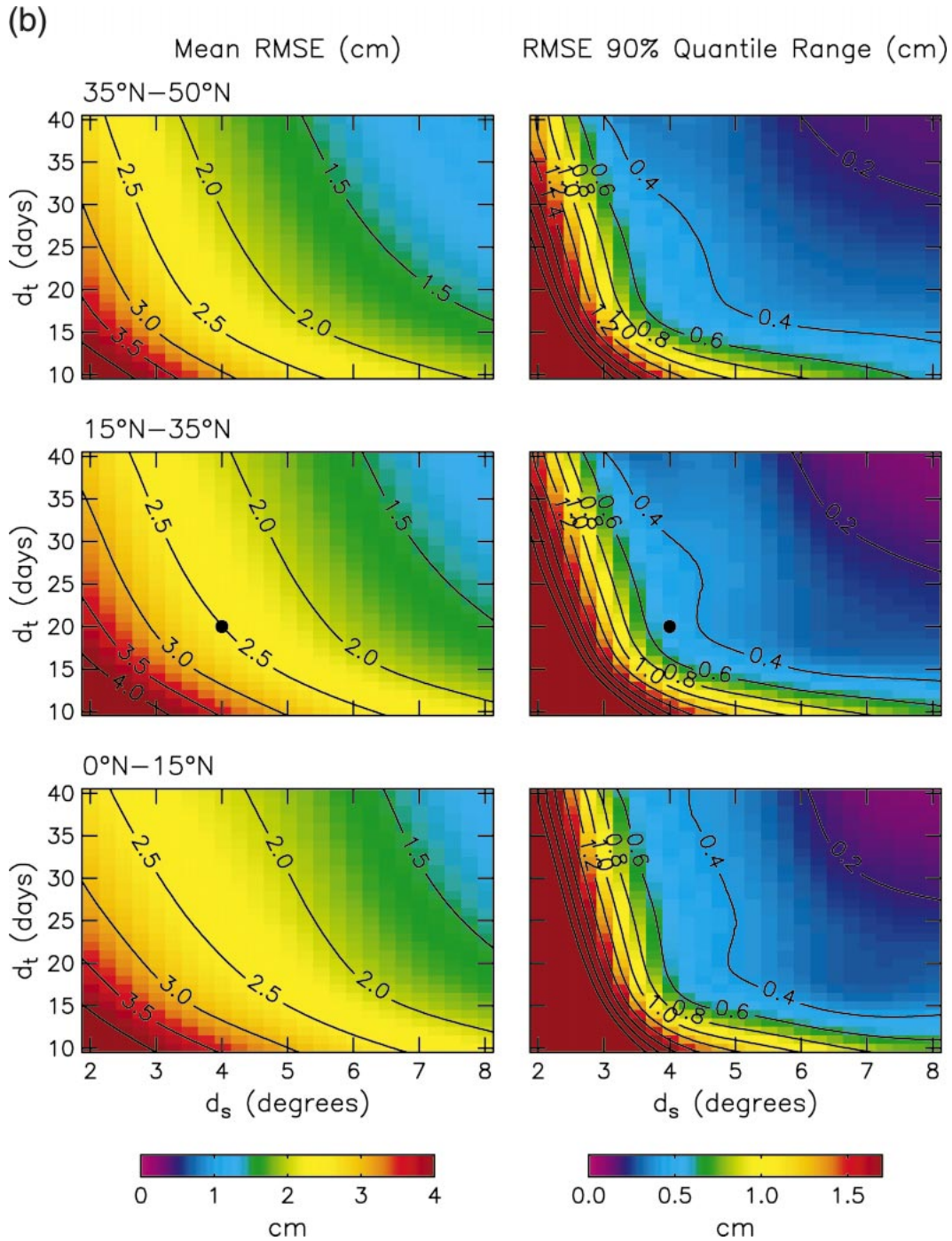
FIG. 13b. As in Fig. 13a except for the case of *ENVISAT* orbit errors with a standard deviation of 6 cm.

nearly all of the sampling patterns considered here. A notable exception is the case of the tandem T/P–*Jason* mission with 0.75° ground track spacing considered in section 3c for which the threshold tolerance of inhomogeneity of rmse is an issue in the Tropics. Inhomogeneity of the mapping errors is also an issue for a tandem T/P–*Jason* sampling pattern with evenly spaced ground tracks and 0-day offset when SSH fields are

constructed in the Tropics with small spatial and temporal smoothing (see section 3b).

4. Scientific benefits of a tandem mission with evenly spaced ground tracks

Of the three tandem T/P–*Jason* altimeter sampling patterns considered in section 3, it was shown that the
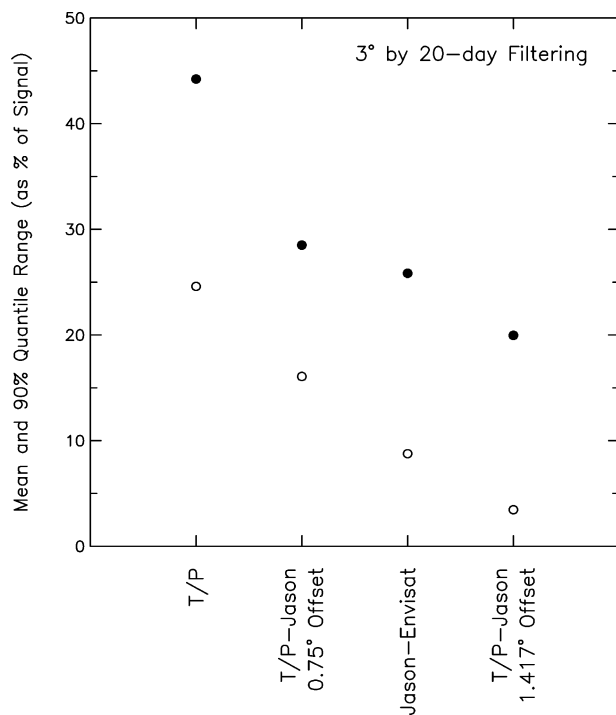
FIG. 14. The average values (solid circles) and the 90% quantile ranges of variation (open circles) of the rmse of SSH fields constructed in the subtropical latitude band from various altimeter sampling patterns for the case of smoothing with a filter cutoff wavelength and period of 3° by 20 days, corresponding approximately to the filtering properties of 1.8° by 12-day block averages. The average and 90% quantile range of rmse are expressed as percentages of the signal standard deviation. The average and 90% quantile values are somewhat higher in the tropical latitude band and lower in the subpolar latitude band.

sampling pattern with evenly spaced ground tracks and 5-day offset would yield the best resolution capability for mapping the SSH field. The parallel-track tandem mission with 0.75° ground track separation would yield significantly lower resolution SSH maps constructed from the combined T/P and *Jason* data.

High-resolution mapping of SSH is not the only consideration in the selection of the sampling pattern for a tandem T/P–*Jason* mission. Another potentially important application is the estimation of surface geostrophic velocity from the tandem altimeter dataset. Leeuwenburgh and Stammer (2002) argue that the parallel-track method applied to tandem T/P–*Jason* data with a 0.75° track separation and a 0-day offset is capable of providing velocity estimates with accuracy that is comparable to, and possibly better than, the accuracy of estimates obtained by the crossover method. They suggest that the high along-track resolution available from the parallel-track method will be useful for determining the along-track wavenumber spectrum of geostrophic velocity and other applications. Because of the sensitivity of the accuracy of parallel-track estimates of geostrophic velocity to the convergence of satellite ground tracks at high latitudes, they note that application of the
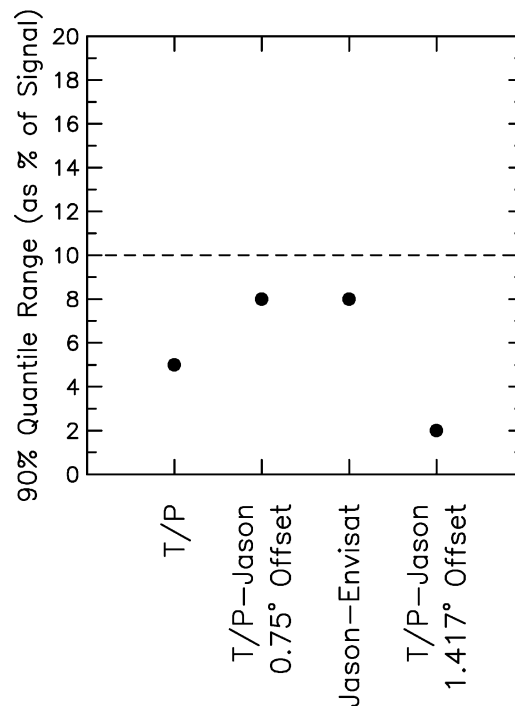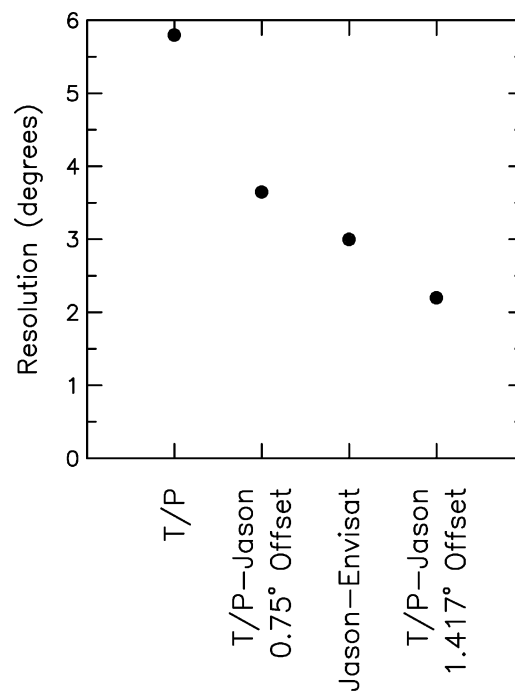

FIG. 15. (top) The filter cutoff wavelengths defining the resolution capability of SSH fields constructed in the subtropical latitude band from various altimeter sampling patterns based on the threshold criterion of 25% of the signal standard deviation for the average mapping error. (bottom) The corresponding 90% quantile ranges of variation of rmse expressed as a percentage of the signal standard deviation. The tandem T/P–*Jason* sampling pattern with evenly spaced ground tracks corresponds to the case of 5-day offset and the tandem *Jason–ENVISAT* sampling patterns correspond to the case of 4-cm *ENVISAT* orbit errors.
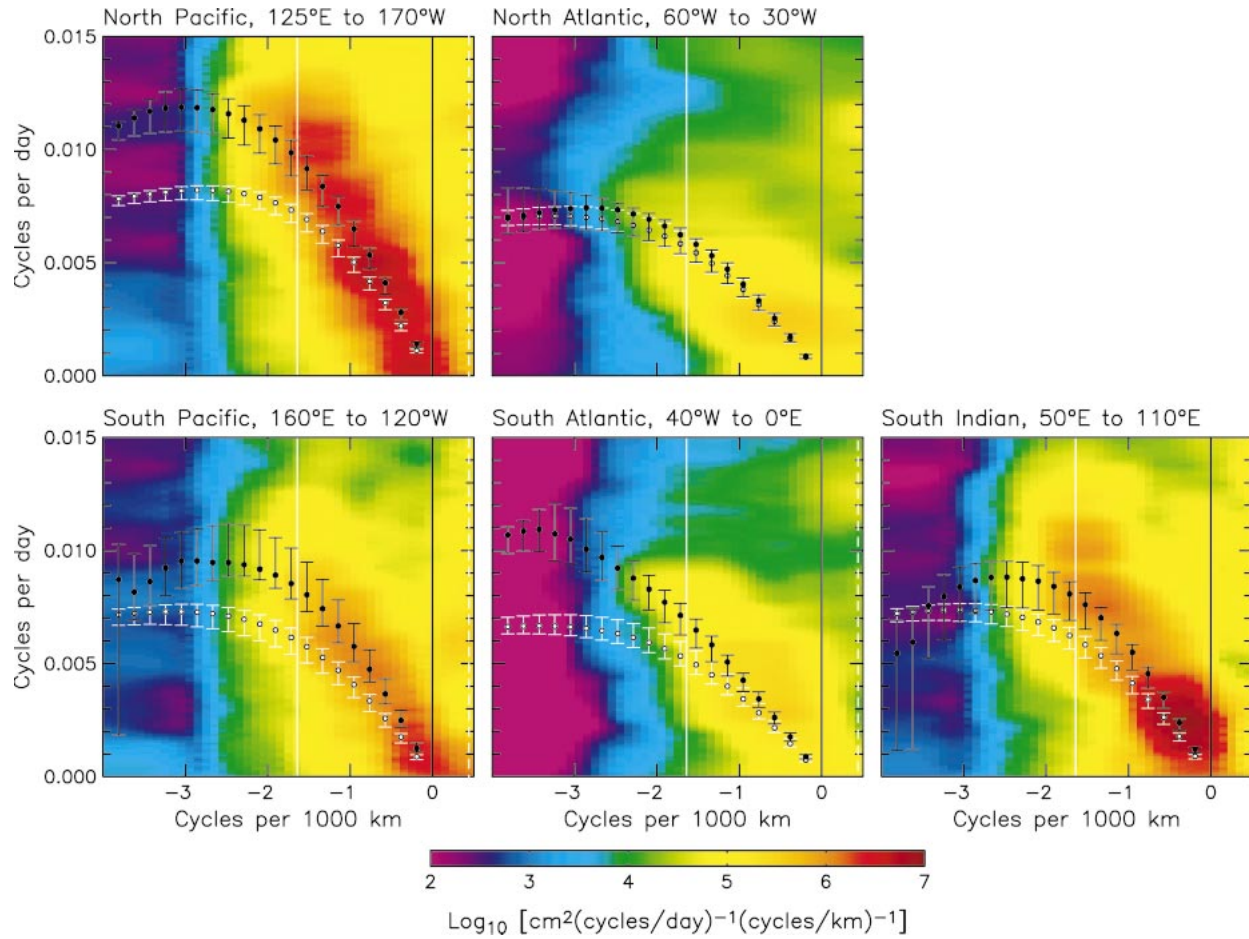
FIG. 16. Wavenumber-frequency spectra computed from 9 yr of T/P data along 24° latitude over the longitude ranges indicated at the top of each panel. Each spectral estimate was band averaged in space and time to obtain 18 degrees of freedom. The dispersion relation computed from the eigenvalue problems for the classical theory with zero mean background flow and the extended theory of Killworth et al. (1997) that includes the baroclinic background mean flow are shown by the open and solid circles, respectively. The error bars correspond to estimates of the 75% confidence intervals for the estimated dispersion relations. The vertical white lines show the wavenumber cutoff associated with the 6° smoothing applied to the T/P data.

method outside of the subtropical and midlatitude regions will require a reduction of residual orbit errors to 1 cm or less.

Using a different approach to investigate the accuracy of parallel-track estimates of geostrophic velocity, we have found that they are subject to substantial errors that vary between the components and with latitude (Schlax and Chelton 2003). We also feel that further study of the latitudinally varying filtering properties of the parallel-track method is required before committing to its use for high-resolution along-track wavenumber spectral analysis of geostrophic velocity.

On the basis of the SSH mapping results presented in section 3 and the conclusions of Leeuwenburgh and Stammer (2002) and Schlax and Chelton (2003) concerning the limitations of velocity estimates derived from altimeter data, we believe that the interleaved sampling pattern with evenly spaced ground tracks would have a beneficial impact on a wider range of scientific

applications of altimeter data than would a tandem mission dedicated to obtaining high-resolution, along-track velocity estimates from the parallel-track method. Two examples are summarized in this section. The first considers the benefits of the improved spatial resolution of SSH fields for investigation of the wavenumber-frequency spectral characteristics of ocean Rossby waves. The second considers the benefits of geostrophic velocity estimates at the crossover points of an evenly spaced, interleaved sampling pattern for investigation of the effects of eddy Reynolds stresses on the mean and slowly varying ocean circulation.

a. Rossby wave dispersion characteristics

Analysis of the longitude–time structure of SSH variability from the first 3 yr of T/P data by Chelton and Schlax (1996) showed that westward propagation is nearly ubiquitous over the World Ocean. A more recent
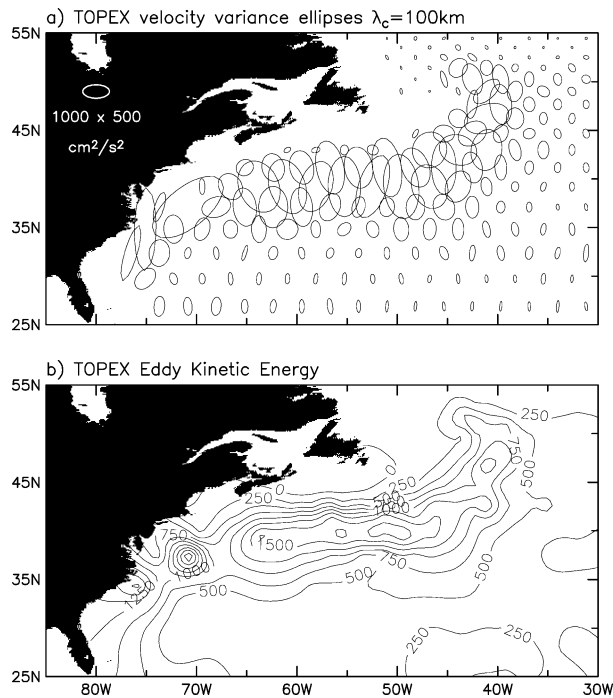
FIG. 17. (a) Velocity variance ellipses based on geostrophic velocity estimates computed by the crossover method from T/P data at the crossovers of ascending and descending ground tracks, and (b) the associated eddy kinetic energy in units of cm² s⁻².
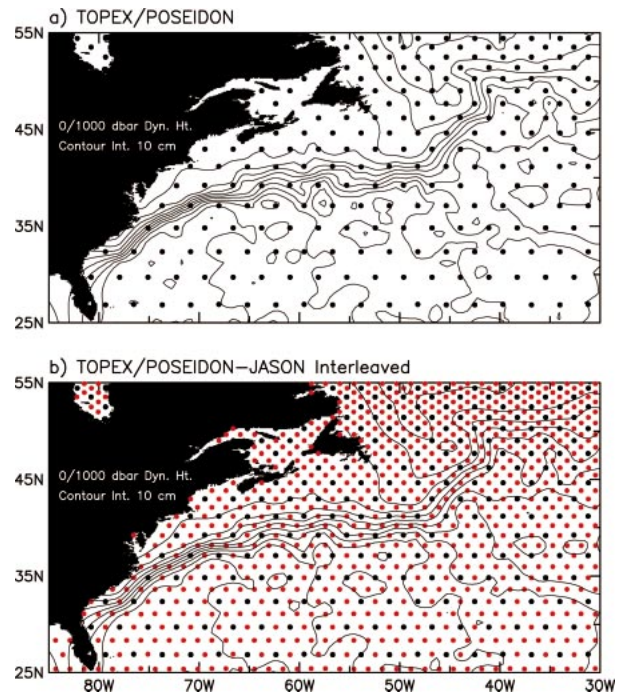

FIG. 18. The locations of the crossovers of ascending and descending ground tracks from (a) a single altimeter in the T/P orbit configuration, and (b) an interleaved tandem orbit configuration with evenly spaced ground tracks. The red dots in (b) correspond to the additional crossover points afforded by the tandem mission. The contours in both panels represent the dynamic height of the sea surface relative to a reference level of 1000 db computed from the Lozier et al. (1995) hydrographic dataset.

global synthesis of westward-propagating SSH signals from 7 yr of T/P data confirms the results of the earlier analysis (Fu and Chelton 2001). The propagation speeds decrease with increasing latitude in a manner that is qualitatively but not quantitatively consistent with the classical theory for oceanic Rossby waves. Westward phase speeds estimated from the T/P data are systematically higher than the phase speeds predicted from the classical theory. The discrepancies between the observations and the classical theory generally increase with increasing latitude, differing by more than a factor of 2 at 40° latitude [see Fig. 5 of Chelton and Schlax (1996) and Fig. 14 of Fu and Chelton (2001)].

The apparent insufficiency of the classical theory has stimulated a great deal of interest in Rossby wave dynamics. Since Rossby waves are the mechanism by which the open ocean adjusts to wind stress, heat flux, and eastern boundary forcing, it is important to understand the reason for the discrepancies between the observed and predicted westward phase speeds of oceanic Rossby waves. Ocean general circulation models that are currently under development for climate studies cannot be considered useful unless they accurately represent the observed Rossby wave phase speeds, thus correctly modeling the transient adjustment time of the ocean. An overview of theoretical attempts to account for the apparent Rossby wave speedup is given in section 3.4.5 of Fu and Chelton (2001). The most promising explanation to date appears to be that proposed by Killworth

et al. (1997), who suggested that the speedup occurs because of the modification of free Rossby wave modes by vertically sheared mean currents.

The empirical and theoretical studies of Rossby wave propagation that have been conducted thus far have focused almost entirely on the long-wavelength, low-frequency nondispersive regime. The adequacies or inadequacies of the various theories that have been proposed to explain the fast observed westward phase speeds are likely to become most apparent when the focus shifts to the full wavenumber-frequency spectral characterization of the westward propagation. Spatial resolution is the most important limiting factor for wavenumber-frequency spectral analysis of SSH data from a single altimeter in the T/P orbit. The results of section 3a indicate that the resolution capability of SSH fields constructed from a single altimeter in the T/P orbit is about 6° in longitude and latitude by 20 days at middle and low latitudes; the spatial resolution capability improves slightly to about 4.5° in the subpolar latitudes (see Fig. 5).

Examples of wavenumber-frequency spectra of SSH computed along 24° latitude in each of the ocean basins from 6° by 60-day smoothed SSH fields are shown in Fig. 16. The 60-day filter cutoff was chosen to eliminate contamination of the SSH fields by tidal errors; the most

energetic tidal signals all alias into periods shorter than about 60 days (Chelton et al. 2001). A 60-day period corresponds to a frequency of 0.016 cpd, which is higher than the maximum frequency displayed the figures. The solid vertical white line in each panel corresponds to the 6° zonal filter cutoff of the loess smoothed SSH fields. The apparent decrease of the energy of SSH variability at larger negative zonal wavenumbers is due to attenuation of these short scales by the 6° zonal smoothing.

Over the range of wavenumbers resolved in SSH fields constructed from T/P data, the wavenumber-frequency spectral characteristics along 24° latitude exhibit a remarkable quality: the bands of energetic SSH variability fall very nearly along straight lines in wavenumber-frequency space. This indicates that the westward propagation of SSH signals is essentially nondispersive over the full range of wavenumbers resolved by the T/P sampling pattern.

The eigenvalue problem derived by Killworth et al. (1997) for the case of nondispersive Rossby waves is extended by Fu and Chelton (2001) to include the dependence on zonal wavenumber. The dispersion relations from the classical theory and the extended Killworth et al. (1997) shear-modified theory are shown in Fig. 16 by the open and solid circles, respectively. It is clear from these plots that the wavenumbers and frequencies of energetic SSH variability are in much closer agreement with the Killworth et al. (1997) theory than with the classical theory. It is also apparent that a comprehensive test of the Killworth et al. (1997) theory will require knowledge of the spectral characteristics of SSH variability at larger negative wavenumbers; the Killworth et al. (1997) theory becomes dispersive for the wavelengths shorter than the 6° of longitude that are not well resolved in SSH fields constructed from the T/P sampling pattern. Moreover, the dispersion relations for the Killworth et al. (1997) theory and the classical theory become progressively more distinct at these shorter wavelengths.

Assessment of the Killworth et al. (1997) theory, as well as of the other theories that have been proposed to explain the observed Rossby wave phase speeds, thus requires SSH fields with zonal spatial resolution higher than can presently be resolved from T/P data alone. The results of section 3b indicate that an interleaved tandem T/P–*Jason* mission with evenly spaced ground tracks would allow mapping of the SSH field with a zonal resolution of about 2.2° at middle and low latitudes. This would extend the wavenumber range of the spectra of SSH variability beyond the minimum wavenumbers plotted in Fig. 16. Since the periodicities of the variability in the short wavenumber regime of interest are about 100 days, we believe that a 1-yr tandem mission would provide sufficient statistical reliability, although a longer record length would be much more desirable. The extended range of the wavenumber-frequency spectral estimates would enable a quantitative test of the adequacy of the various theories for fast Rossby waves. If the Killworth et al. (1997) theory shown by the solid circles in Fig. 16 is the mechanism for Rossby wave speedup, then the band of wavenumbers and frequencies of the most energetic SSH variability should flatten for zonal wavelengths shorter than the 6° limitation of SSH fields constructed from T/P data. This corresponds to zonal wavenumbers with negative values larger in magnitude than the filter cutoff wavenumber indicated by the vertical solid white lines in Fig. 16.

b. Eddy kinetic energy and Reynolds stresses

Although the coarse grid of crossover points in the T/P sampling pattern is limiting, the crossover technique for estimating surface geostrophic velocity nonetheless provides useful estimates of the velocity variance, especially in the midlatitude regions of most energetic eddy variability. An example of the velocity variance ellipses formed from the variances of the two orthogonal velocity components and the cross covariance between the two components (Preisendorfer 1988; Morrow et al. 1992, 1994; Schlax and Chelton 2003) is shown in Fig. 17a and the associated eddy kinetic energy is shown in Fig. 17b. When multiplied by the water density, the variances and cross covariance have units of force per unit area and represent horizontal fluxes of momentum by the eddy field, the so-called eddy Reynolds stresses. The cross-track velocity estimates from which the orthogonal velocity components were computed for the velocity variances in Fig. 17 were estimated from 9 yr of T/P data based on along-track slopes obtained from least squares fits over nine successive points along the satellite ground track, which corresponds to a filter cutoff wavelength of $\lambda_c \approx 100$ km (Schlax and Chelton 2003).

The velocity variances and eddy kinetic energy in Fig. 17 can be compared with the results obtained by Richardson (1983) from 2°-gridded averages of the velocities of 110 surface drifters. In consideration of the rather coarse spatial resolution of both datasets, and especially of the small number of drifters, the agreement between the geographical distributions of the two estimates of eddy kinetic energy (EKE) is rather remarkable. Both datasets are characterized by a band of large EKE in excess of 1000 cm^2 s^{-2} that extends northeastward from Cape Hatteras to about 45°W where it turns north around Grand Banks and extends to about 50°. The bull's-eyes of locally large EKE at about 34°N, 76°W and 37°N, 71°W in the T/P data are associated with isolated velocity variance ellipses in Fig. 17a. The detailed spatial structures and geographical extents of these regions of energetic variability are not resolved by the T/P sampling pattern.

The agreement between the T/P and drifter estimates of velocity variance ellipses is more difficult to assess. The nature of the anisotropy of the velocity variance (i.e., the elongation and orientation of the ellipses) is

generally similar, although there are some notable discrepancies. For example, the T/P variance ellipses at 34°N, 76°W are rotated about 45° counterclockwise relative to the drifter ellipses near the same location. This and other less significant differences could easily be attributed to inadequate sampling in the drifter results because of the small number of observations from which the velocity statistics were computed.

The anisotropy of the velocity variability evident in Fig. 17a is important to ocean dynamics. In baroclinically unstable flow regimes such as the Gulf Stream, eddies force the mean and slowly varying flow by a cross-stream convergence of alongstream momentum, thus accelerating the mean flow [e.g., Cronin (1996); see also Fig. 7.3.1 of Pedlosky (1987)]. The convergence or divergence of eddy momentum flux can be determined from horizontal gradients of the Reynolds stresses. The coarse 2.834° staggered grid of crossover points from a single altimeter in the T/P orbit is severely restrictive in this regard (Fig. 18a); the approximate 3° latitudinal separations of the crossover points at midlatitudes (see Fig. 4 of GCS97) is too coarse relative to the width of the Gulf Stream to obtain useful estimates of the eddy convergence of momentum.

A byproduct of the sampling pattern of an interleaved tandem T/P–*Jason* altimeter sampling pattern with evenly spaced ground tracks is a fourfold increase in the number of crossovers of ascending and descending ground tracks. Such a tandem mission would result in a staggered grid of crossover points with 1.417° longitudinal spacing and about 1.5° latitudinal spacing at midlatitudes (Fig. 18b). This quadrupling of the number of crossover points would greatly enhance the ability to investigate eddy–mean flow interaction from altimeter data.

In principle, the tandem *Jason–ENVISAT* mission could provide an even more dense grid of crossovers for analysis of Reynolds stress gradients. Because of the complexity of the space–time characteristics of the uncoordinated *Jason* and *ENVISAT* sampling pattern, however, the effects of sampling errors on crossover estimates of geostrophic velocity are far more complicated than from a tandem T/P–*Jason* mission. The higher inclination of the *ENVISAT* orbit results in much larger errors in the meridional velocity component. The longer 35-day repeat period results in larger temporal interpolation errors from the time separations between *ENVISAT–ENVISAT* crossovers (which can differ by as much as 17.5 days) and *Jason–ENVISAT* crossovers (which can differ by as much as 12.5 days). Moreover, the numbers of crossovers within a given time span differ for *Jason–Jason, Jason–ENVISAT,* and *ENVISAT–ENVISAT* crossovers and thus vary in a complex manner geographically. This results in an additional source of sampling error that does not exist for a tandem altimeter mission with a coordinated sampling pattern (i.e., matched orbit repeat periods).

It is noteworthy that the tandem mission with 0.75°

offset between neighboring T/P and *Jason* ground tracks that has been suggested by Leeuwenburgh and Stammer (2002) as an optimal sampling pattern for parallel-track estimates of geostrophic velocity would not significantly improve studies of eddy–mean flow interaction. The method yields Reynolds stress estimates at closely spaced intervals along the centerline between the parallel tracks. However, the orthogonal components of the Reynolds stress gradient field that effects the momentum flux in eddy–mean flow interaction cannot be estimated with the same high along-track resolution. The gradients could be estimated from Reynolds stresses on the staggered grid consisting of the crossovers and the midpoints between the crossovers of intersecting centerlines. This is exactly the same grid obtainable from the crossover method applied to tandem T/P–*Jason* data with evenly spaced ground tracks.

Because of the lack of improvement in spatial resolution, and the fact that the parallel-track estimates of geostrophic velocity offer no great improvement in precision over the crossover method for realistic long-wavelength measurement and orbit errors (Schlax and Chelton 2003). The parallel-track method appears to be no more useful than the crossover method for the investigation of eddy–mean flow interaction. Indeed, the parallel-track method would be less useful if the residual long-wavelength measurement and orbit errors were to exceed 2 cm.

5. Conclusions

The value of continuing the T/P mission for as long as the dual-frequency altimeter and other system components continue to function well is self-evident. After a 7-month calibration and validation period following the December 2001 launch of *Jason,* T/P was maneuvered into an interleaved orbit in which neighboring parallel ground tracks with 1.417° longitudinal separation are sampled essentially simultaneously by T/P and *Jason.* This tandem mission was established on 16 September 2002. The improved spatial resolution of SSH fields constructed from the combined T/P and *Jason* datasets with this coordinated 10-day exact-repeat sampling pattern will enable scientific investigations that have not heretofore been possible from past and present altimeter datasets. Moreover, the future launch of the *Jason* follow-on altimeter with a planned launch in 2007 will provide another opportunity for a coordinated tandem altimeter mission. The specifics of a coordinated tandem mission therefore merit careful consideration. The primary purpose of this study has been to evaluate two potential tandem T/P–*Jason* orbit configurations: an interleaved sampling pattern consisting of evenly spaced ground tracks, and a 0.75° offset between simultaneous measurements by T/P and *Jason* that has been suggested by Leeuwenburgh and Stammer (2002) as the optimal track separation for estimates of geostrophic velocity by the parallel-track method.

The results presented here are based on an extension of the technique that we have previously used to assess the resolution capability of smoothed SSH fields constructed from various altimeter sampling patterns (CS94 and GCS97). Our earlier analyses considered only the effects of sampling errors and restricted attention to the altimeter sampling patterns and signal autocorrelation function at midlatitudes. The effects of measurement errors that were neglected in our earlier studies become important when considering the ERS and *ENVISAT* altimeters for which the orbit errors are about a factor of 2 larger than for T/P and *Jason*. The formalism outlined in section 2 includes the effects of both sampling and measurement errors. The present study also adopts a more realistic representation of the signal autocorrelation function that allows an assessment of latitudinally varying resolution capability of the various altimeter sampling patterns. The mapping errors are assessed here from the total root-mean-squared error of quadratic loess smoothed estimates of SSH compared with the best possible smoothed estimates that could be obtained by the quadratic loess smoother if the observations were continuously distributed in space and time.

The spatial and temporal resolution capabilities of SSH fields constructed from the two potential tandem T/P–*Jason* sampling patterns were quantified in sections 3b and 3c. The resolution capability is assessed from the mean value and the spatial and temporal variability of the root-mean-squared errors computed over a representative collection of estimation times and locations. To identify the filter cutoff wavelength and period that define the resolution capability of SSH fields constructed from each altimeter sampling pattern, we have adopted a threshold values of 25% of the signal standard deviation σ_h for the overall average rmse and a threshold value of 10% of σ_h for the 90% quantile range of rmse variability. The wavenumber-frequency distribution of σ_h^2 is specified by the Gaussian form assumed here for the space–time autocorrelation function of SSH.

While a 0.75° offset between the T/P and *Jason* ground tracks in the tandem mission would offer an improvement over the resolution capability of SSH fields constructed from a single altimeter in the T/P orbit (an increase in resolution from about 6° to about 3.7° of longitude and latitude within the subtropical latitude band), the improvement falls far short of the 2.2° resolution capability of the interleaved tandem sampling patterns with evenly spaced ground tracks considered in section 3b. The interleaved tandem sampling pattern is thus superior for global mapping of the SSH field. The filter cutoff wavelength and period of 2.2° by 20 days corresponds approximately to the filtering properties of 1.3° by 12-day block averages.

We also assessed the resolution capability of SSH fields constructed from the tandem *Jason–ENVISAT* sampling pattern in section 3d. Because of the lack of coordination of the orbit configurations (66° inclination with 10-day repeat for *Jason* and 98° inclination with

35-day repeat for *ENVISAT*) and because of the larger orbit errors for *ENVISAT,* the mapping resolution capability of the tandem dataset falls short of the 2.2° resolution obtainable from the tandem T/P–*Jason* sampling pattern with evenly spaced interleaved ground tracks. For *ENVISAT* orbit errors with a standard deviation of 4 cm, the resolution capability of the tandem *Jason–ENVISAT* sampling pattern would be about 3°. If the *ENVISAT* orbit errors are as large as 6 cm, the spatial resolution of the SSH fields would be degraded to about 4°.

The scientific value of an evenly spaced, interleaved tandem T/P–*Jason* sampling pattern was discussed in section 4 by summarizing two specific applications that would benefit greatly from the doubling of the spatial resolution of the SSH field and the quadrupling of the number of crossovers afforded by the evenly spaced, interleaved sampling pattern. The higher spatial resolution would allow wavenumber-frequency spectral analysis of SSH fields at high wavenumbers where competing theories for Rossby wave dispersion differ most significantly. Since Rossby waves are the means by which the large-scale ocean circulation adjusts to atmospheric and eastern boundary forcing, a theoretical understanding of Rossby wave dynamics is important to understanding ocean climate variability on timescales of the order of a month and longer. The other scientific application considered here is the estimation of Reynolds stresses and eddy momentum flux convergence and divergence at the crossovers of ascending and descending ground tracks. The fourfold increase and regular spacing of the crossovers in the evenly spaced sampling pattern of an interleaved tandem T/P–*Jason* mission would yield important insight into the role of eddy momentum flux convergences and divergences in the large-scale ocean circulation.

REFERENCES

Bretherton, F. P., R. E. Davis, and C. B. Fandry, 1976: A technique for objective analysis and design of oceanographic experiments applied to MODE-73. *Deep-Sea Res.,* **23,** 559–582.

Chelton, D. B., and M. G. Schlax, 1994: The resolution capability of an irregularly sampled dataset with application to *GEOSAT* altimeter data. *J. Atmos. Oceanic Technol.,* **11,** 534–550.

——, and ——, 1996: Global observations of oceanic Rossby Waves. *Science,* **272,** 234–238.

——, R. A. de Szoeke, M. G. Schlax, K. El Naggar, and N. Siwertz,

1998: Geographical variability of the first-baroclinic Rossby radius of deformation. *J. Phys. Oceanogr.,* **28,** 433–460.

——, J. C. Ries, B. J. Haines, L.-L. Fu, and P. S. Callahan, 2001: Satellite altimetry. *Satellite Altimetry and the Earth Sciences: A Handbook for Techniques and Applications,* L.-L. Fu and A. Cazenave, Eds., Academic Press, 1–131.

Cleveland, W. S., and S. J. Devlin, 1988: Locally weighted regression: An approach to regression analysis by local fitting. *J. Amer. Stat. Assoc.,* **83,** 596–610.

Cronin, M., 1996: Eddy–mean flow interaction in the Gulf Stream at 68°W. Part II: Eddy forcing on the time-mean flow. *J. Phys. Oceanogr.,* **26,** 2132–2151.

Fu, L.-L., and D. B. Chelton, 2001: Large-scale ocean circulation. *Satellite Altimetry and the Earth Sciences: A Handbook for Techniques and Applications,* L.-L. Fu and A. Cazenave, Eds., Academic Press, 133–169.

Greenslade, D. J. M., D. B. Chelton, and M. G. Schlax, 1997: The midlatitude resolution capability of sea level fields constructed from single and multiple satellite altimeter datasets. *J. Atmos. Oceanic Technol.,* **14,** 849–870.

Killworth, P. D., D. B. Chelton, and R. A. de Szoeke, 1997: The speed of observed and theoretical long extra-tropical planetary waves. *J. Phys. Oceanogr.,* **27,** 1946–1966.

Leeuwenburgh, O., and D. Stammer, 2002: Uncertainties in altimetry-based velocity estimates. *J. Geophys. Res.,* **107,** 3175, doi:1029/2001JC000937.

Le Traon, P.-Y., and G. Dibarboure, 1999: Mesoscale mapping capabilities of multiple-satellite altimeter missions. *J. Atmos. Oceanic Technol.,* **16,** 1208–1223.

Lozier, M. S., W. B. Owens, and R. G. Curry, 1995: The climatology of the North Atlantic. *Progress in Oceanography,* Vol. 36, Pergamon, 1–44.

Morrow, R., J. Church, R. Coleman, D. Chelton, and N. White, 1992: Eddy momentum flux and its contribution to the Southern Ocean momentum balance. *Nature,* **357,** 482–484.

——, ——, ——, and ——, 1994: Surface eddy momentum flux and velocity variances in the Southern Ocean from *Geosat* altimetry. *J. Phys. Oceanogr.,* **24,** 2050–2071.

Pedlosky, J., 1987: *Geophysical Fluid Dynamics.* Springer-Verlag, 710 pp.

Preisendorfer, R. W., 1988: *Principal Component Analysis in Meteorology and Oceanography.* Elsevier, 425 pp.

Richardson, P. L., 1983: Eddy kinetic energy in the North Atlantic from surface drifters. *J. Geophys. Res.,* **88,** 4355–4367.

Schlax, M. G., and D. B. Chelton, 1992: Frequency domain diagnostics for linear smoothers. *J. Amer. Stat. Assoc.,* **87,** 1070–1081.

——, and ——, 2003: The accuracies of crossover and parallel-track estimates of geostrophic velocity from TOPEX/Poseidon and Jason altimeter data. *J. Atmos. Oceanic Technol.,* **20** 1196–1211.

——, ——, and M. H. Freilich, 2001: Sampling errors in wind fields constructed from single and tandem scatterometer datasets. *J. Atmos. Oceanic Technol.,* **18,** 1014–1036.

Shen, C. Y., J. C. McWilliams, B. A. Taft, C. C. Ebbesmeyer, and E. J. Lindstrom, 1986: The mesoscale spatial structure and evolution of dynamical and scalar properties observed in the northwestern Atlantic Ocean during the POLYMODE Local Dynamics Experiment. *J. Phys. Oceanogr.,* **16,** 454–482.

Stammer, D., 1997: Global characteristics of ocean variability estimated from regional *TOPEX/Poseidon* altimeter measurements. *J. Phys. Oceanogr.,* **27,** 1743–1769.

——, and C. Dieterich, 1999: Space-borne measurements of the time-dependent geostrophic ocean flow field. *J. Atmos. Oceanic Technol.,* **16,** 1198–1207.

Tai, C.-K., 1998: On the spectral ranges that are resolved by a single satellite in exact-repeat orbit. *J. Atmos. Oceanic Technol.,* **15,** 1459–1470.

——, 2001: The resolving power of a single exact-repeat altimetric satellite or a coordinated constellation of satellites: The definitive answer and data compression. NOAA Tech. Rep. NESDIS 100, 8 pp.